Title

Sources of Subseasonal-To-Seasonal Predictability of Atmospheric Rivers and Precipitation in the Western United States

Journal

Journal of Geophysical Research: Atmospheres, 126(6)

ISSN

2169-897X

Authors

Huang, Huanping
Patricola, Christina M
Bercos-Hickey, Emily
et al.

Publication Date

2021-03-27

DOI

10.1029/2020jd034053

Peer reviewed

JGR Atmospheres

RESEARCH ARTICLE
10.1029/2020JD034053

Special Section:
Atmospheric Rivers: Intersection of Weather and Climate

Sources of Subseasonal-To-Seasonal Predictability of Atmospheric Rivers and Precipitation in the Western United States

Huanping Huang[1], Christina M. Patricola[2,1], Emily Bercos-Hickey[1], Yang Zhou[1], Alan Rhoades[1], Mark D. Risser[1], and William D. Collins[1,3]

[1]Climate and Ecosystem Sciences Division, Lawrence Berkeley National Laboratory, Berkeley, CA, USA, [2]Department of Geological and Atmospheric Sciences, Iowa State University, Ames, IA, USA, [3]Department of Earth and Planetary Science, University of California, Berkeley, Berkeley, CA, USA

Key Points:

- The El Niño/Southern Oscillation (ENSO)-atmospheric river (AR) relationship depends on ENSO index, with enhanced landfalling AR activity during extreme El Niño
- Madden-Julian oscillation (MJO) leads to significant landfalling AR and precipitation anomalies in large-ensembles, but observations are too short to show this signal
- ENSO modulates the MJO-AR relationship, thus consideration of concurrent climate modes could improve seasonal hydroclimate prediction

Supporting Information:

- Supporting Information S1

Correspondence to:
H. Huang,
huanpinghuang@lbl.gov

Citation:
Huang, H., Patricola, C. M., Bercos-Hickey, E., Zhou, Y., Rhoades, A., Risser, M. D., & Collins, W. D. (2021). Sources of subseasonal-to-seasonal predictability of atmospheric rivers and precipitation in the western United States. *Journal of Geophysical Research: Atmospheres*, *126*, e2020JD034053. https://doi.org/10.1029/2020JD034053

Received 9 OCT 2020
Accepted 4 MAR 2021

Abstract Atmospheric rivers (ARs) account for a large portion of winter precipitation in the western US. To evaluate the sources of AR and precipitation predictability at subseasonal-to-seasonal timescales, we examine the relationships between two climate modes, the El Niño/Southern Oscillation (ENSO) and Madden-Julian oscillation (MJO), and winter hydroclimate in the western US. Our analysis uses a large ensemble of the Weather Research and Forecast (WRF) model simulations from 1981 to 2017, facilitating the assessment of uncertainty in climate mode-AR relationship due to climate variability and short length of observations. Over the North Pacific basin, we find ENSO-related latitudinal shifts of ARs, but ENSO has little effect on basin-wide averaged AR frequency. Over the western US, there is some uncertainty in the ENSO-AR connection due to the impacts of ENSO indices and datasets. However, extreme El Niño events defined by the ENSO longitude index are consistently linked to increased landfalling AR activity. The MJO can lead to significantly enhanced or suppressed landfalling AR activity in the large-ensembles, depending on the phase of MJO and time lag, while observations are too short in length to robustly show this signal. ENSO substantially modulates the MJO-AR relationship, triggering variegated responses of landfalling ARs and AR precipitation in La Niña and El Niño years. Our findings highlight the need to evaluate concurrent effects of different climate modes on ARs and precipitation, and may shed light on a path toward more accurate subseasonal-to-seasonal prediction of ARs and precipitation over the western US.

1. Introduction

Atmospheric rivers (ARs) are synoptic-scale long and narrow bands of water vapor transport sourced from tropical and/or extratropical regions (American Meteorological Society, 2019; Zhu & Newell, 1998). They are responsible for more than 90% of poleward water vapor transport (Zhu & Newell, 1998), highlighting their importance to hydrological cycle in midlatitudes, especially at the west coasts of continents (Payne et al., 2020; Shields et al., 2018). In the coastal states of the western US, ARs contribute to a large portion of total precipitation, especially in the form of heavy precipitation and during the cool season (Dettinger et al., 2011; Lavers & Villarini, 2015; Rutz & Steenburgh, 2012; Rutz et al., 2014). For instance, Rutz et al. (2014) reported that over 60% of cool season total precipitation is associated with ARs along the coast in northern California, Oregon, and Washington. The percentage contributions by ARs decrease in southern California and farther inland in these states. However, interannual variability of precipitation is also high in the region, as exemplified by the recent shift from drought in 2012–2016 to an extremely wet winter 2016–2017 in California, which was largely associated with variability in landfalling ARs (Swain et al., 2018; Wang et al., 2017). Thus, accurate subseasonal-to-seasonal prediction of AR activity and associated precipitation is critically important to assist governments and stakeholders to manage water resources and drought and flood risks.

Previous studies have focused on climate modes as the source of AR prediction skill and investigated their modulation on ARs over the North Pacific and western US (Baggett et al., 2017; DeFlorio et al, 2018, 2019; Guan & Waliser, 2015; Mundhenk et al, 2016, 2018; Pan et al., 2019; Payne & Magnusdottir, 2014). The El Niño/Southern Oscillation (ENSO) is the climate mode frequently used in seasonal hydroclimate prediction because it strongly influences AR location, frequency, and intensity, and therefore precipitation (DeFlorio

et al., 2018; Patricola et al., 2020; Zhou & Kim, 2018). While the displacements of AR activity by ENSO phase in the North Pacific were consistently found, there exist some disagreements on the modulation of ENSO on landfalling ARs over the western US. For example, Mundhenk et al. (2016) and Guan and Waliser (2015) found a poleward increase in North Pacific AR frequency in La Niña periods, and an opposite change during the El Niño phase. This is associated with a weakened (enhanced) Aleutian Low and poleward (equatorward) shifted subtropical jet in the La Niña (El Niño) phase (Kim et al., 2017; Payne & Magnusdottir, 2014). In the western US, Guan and Waliser (2015) concluded that ENSO played a negligible role in affecting landfalling AR frequency and precipitation. However, others found more frequent landfalling ARs in El Niño periods than in La Niña periods (Kim et al., 2017; Mundhenk et al., 2016; Payne & Magnusdottir, 2014). It is worth noting that the qualitative assessments were based on a short period of observations (typically under 40 years in reanalysis) and limited number of El Niño/La Niña events. For winter precipitation, Patricola et al. (2020) demonstrated that the ENSO Longitude Index (ELI), a new metric that captures the diversity of ENSO's spatial variations (Williams & Patricola, 2018), served as a more useful predictor of western US precipitation variability than the commonly used Niño 3.4 index, especially during strong El Niño years. But ELI's value in improving the predictive skill of ARs and associated precipitation has not been explored.

The Madden-Julian oscillation (MJO) is another climate mode that has received considerable attention for its important role in altering configurations of the Pacific jets and moisture transport, and thus affects the predictive skill of AR and precipitation at subseasonal scale (DeFlorio et al., 2019; Nardi et al., 2020; Stan et al., 2017). Nevertheless, there is little consensus on the relationship between MJO and landfalling ARs over the western US. For instance, Harris and Carvalho (2018) found more frequent landfalling ARs during MJO phases 1 and 7, followed by phases 3 and 6. Guan et al. (2012) and Guan and Waliser (2015) concluded that the MJO exerted little influence on the western US AR frequency and precipitation during most phases, except for phase 6 when increased ARs and precipitation were documented. In contrast, Mundhenk et al. (2016) found less frequent ARs in the western US during MJO phases 5 and 6. When the time lag effect of MJO was considered, Guan et al. (2012) found no consistent relationship between MJO and AR in California (including the first 10 days following phase 6), but Mundhenk et al. (2018) discovered consistently higher (lower) AR activity in the days following phase 7 (4) in California. When the MJO coexisted with different ENSO phases, the responses of ARs and precipitation to their interactions exhibited a high degree of incoherence (Collow et al., 2020; Mundhenk et al., 2016). The quasi-biennial oscillation (QBO), a dominant mode of tropical stratospheric variability, is shown to modulate MJO convection (Kuma, 1990; Martin et al., 2019; Yoo & Son, 2016) and thus provides subseasonal predictability for ARs and precipitation in the western US (Baggett et al., 2017; Mundhenk et al., 2018; Nardi et al., 2020).

While much work has been done to quantify the empirical relationships between climate modes (ENSO and MJO in particular) and western US hydroclimate, a lack of consensus on ENSO-AR and MJO-AR relationship limits subseasonal-to-seasonal predictive skills on ARs and precipitation. The factors include relatively short observational records, the nonlinear response of ARs to natural modes of climate variability, and uncertainties in AR frequency due to AR detection methods (Mundhenk et al., 2016; Rutz et al., 2019). Furthermore, the influence of climate modes on AR activity varies greatly by location, season, and time scale (Harris & Carvalho, 2018; Mundhenk et al., 2018). The concurrent effects of different climate modes have been shown to modulate precipitation, temperature, tropical cyclones, and atmospheric circulation, thus offering the potential for improved subseasonal-to-seasonal forecasts relative to the climate modes individually (Arcodia et al., 2020; Johnson et al., 2014; Patricola et al., 2014; Roundy et al., 2010). In contrast, their joint influences on ARs and associated precipitation are less thoroughly studied.

Here, we aim to thoroughly evaluate the sources of subseasonal-to-seasonal predictability of ARs and precipitation by investigating the individual and concurrent effects of ENSO events and MJO phases on ARs landfalling in different subregions of the western US during December–February (DJF). Besides the traditional ENSO index defined over a fixed region (i.e., Niño 3.4), we also assess whether ENSO diversity (represented by the ELI) can improve the predictability of landfalling ARs and associated precipitation. Unlike past studies primarily based on reanalysis data, our analysis also leverages a large ensemble of regional climate model (RCM) hindcasts (27 km resolution) over the period 1981–2017 (Patricola et al., 2020). This approach not only enables us to quantify climate mode-AR and AR-precipitation relationships by considering observations/modeling uncertainties due to internal climate variability (Deser et al., 2020; Shields

et al., 2018), but also offers a physically based and systematic assessment of extreme ENSO events' modulation on landfalling ARs and precipitation. Besides ENSO and MJO, we do not include the QBO as another predictor because: (1) the impact of MJO and ENSO interaction on AR and precipitation is more relevant with our research focus and (2) climate models, especially those with low vertical resolution in the upper troposphere and lower stratosphere, have limited capability in simulating QBO (Giorgetta & Roeckner, 2002; Orbe et al., 2020; Richter et al., 2014, 2020). The research questions to be examined are: (1) Can the RCM simulations reproduce the climatology and variability of observation-based ARs and precipitation in the western US from 1981–2017? (2) How does the location and timing of landfalling AR activity and associated precipitation depend on ENSO diversity? (3) What are the influences of MJO phases on AR activity and precipitation, and do ENSO events modulate the MJO-AR relationship?

In the manuscript, Section 2 describes the observations, reanalysis, and RCM simulations used to detect ARs and AR-induced precipitation. Section 3 evaluates the performance of the RCM large ensemble in simulating ARs and precipitation. Section 4 presents the effects of ENSO and MJO on ARs and precipitation in different regions, and discusses the pathway toward improving AR and precipitation prediction skills. Section 5 summarizes concluding remarks and implications for future work.

2. Data and Methods

To detect winter ARs in the North Pacific and western US, we use an observation-based reanalysis and a large ensemble of RCM simulations from 1981–2017, which serve as inputs into an AR detection algorithm. To identify the western US precipitation events associated with ARs, we use a gridded precipitation observation data set and the RCM simulations to extract AR precipitation. Based on the observation-based ENSO and MJO indices, we further explore the effects of sea surface temperatures (SSTs) and atmospheric circulation on ARs and precipitation events. The goal is to evaluate the sources of predictability of ARs and precipitation at subseasonal-to-seasonal timescales. More details on the datasets and methods are described as follows.

2.1. Observations and Reanalysis Data

To detect winter ARs in the historical period 1981–2017, we use the Modern-Era Retrospective analysis for Research and Applications, Version 2 (MERRA2) developed by NASA's Global Modeling and Assimilation Office (Gelaro et al., 2017). This global reanalysis assimilates different sources of observations and provides data from 1980 to present. Its horizontal resolution is 0.5° × 0.625° and it includes 72 vertical levels from Earth's surface to 0.01 hPa. It was utilized as the only data set to implement the Tier 1 experiment in the Atmospheric River Tracking Method Intercomparison Project (Shields et al., 2018). The 6-hourly data was imported into an AR tracking algorithm to detect ARs over time and space, as described in Section 2.3.

Daily observations of precipitation are from the NOAA Climate Prediction Center (CPC) Gauge-Based Unified Precipitation data set (Xie et al., 2010). This gridded data set covers the period from 1948–present and the contiguous United States with a spatial resolution of 0.25°, which is similar to the resolution of RCM simulations.

2.2. Regional Climate Model Simulations

We use a large ensemble of high resolution (27 km) climate simulations 1981–2017 to investigate ARs and precipitation in the western US. High resolution climate data has been shown to better capture ARs and regional precipitation (Hagos et al., 2015, 2016; Shields & Kiehl, 2016; Shields et al., 2018). Furthermore, previous studies on AR predictability primarily used a single reanalysis or small ensemble of global climate model simulations, which cannot address observation or model uncertainties due to internal climate variability. In contrast, the large ensemble-based approach simulates different trajectories of atmospheric response as a function of internal variability alone and estimates physically plausible ways in which ARs can be modulated by low frequency variability (Deser et al., 2020; Shields et al., 2018). Thus, the approach used in the current study may lead to a more robust evaluation of climate mode–AR and AR–precipitation

relationships and provide important implications for the predictability of ARs and associated precipitation over the western US.

The large ensemble RCM data were provided and described by Patricola et al. (2020). The data were generated by downscaling a 6-hourly global reanalysis (NCEP-DOE AMIP-II Reanalysis, 2.5° × 2.5° resolution and 17 pressure levels) with the Weather Research and Forecasting (WRF) model (Powers et al., 2017) version 3.8.1 to a higher resolution of 27 km. SSTs are prescribed by the 0.25° daily NOAA Optimum Interpolation V2 SST (Reynolds et al., 2002). It is worth noting that long-term ENSO diversity is well represented by the ENSO events from 1981 to 2017. We contrasted the distributions of observation-based (ERSSTv5) ENSO longitude index (ELI) during DJFs 1981–2017 and 1854–2020, and find no significant difference between ELIs in the two periods ($p = 0.90$; Figure S1). The model was configured with the following physics options: Single-Moment 3-class scheme (microphysics), Rapid Radiative Transfer Model scheme (radiation), Yonsei University scheme (planetary boundary layer), Kain-Fritsch scheme (cumulus), and Noah land surface model. The parameterizations were selected and used by Patricola et al. (2020) to study the western US hydroclimate variability. The WRF simulations were then run over a region spanning 20°S–60°N and 130°E–60°W and comprised of year-long large ensemble hindcasts from 1981 to 2017. Each hindcast covers a full water year (from October 1 to September 30 of the following year), as well as the month earlier (i.e., September) for initialization and spin-up. There are five ensemble members (initiated on September 1–5) in normal years, and 22–25 ensemble members (typically initiated on September 1–25) for seven designated wet/dry years (1982/1983, 1997/1998, 2012/13, 2013/14, 2014/15, 2015/16, and 2016/17). To better account for observational uncertainty in climate model evaluation (Gibson et al., 2019), we also analyzed the Parameter-elevation Relationships on Independent Slopes Model (PRISM) precipitation observations (Daly et al., 2008) besides the CPC precipitation data set as a comparison.

2.3. Atmospheric River Tracking Algorithm

The Tempest software package (Ullrich & Zarzycki, 2017) was used to detect ARs in the MERRA2 reanalysis and WRF hindcasts. Similar to other AR tracking algorithms, Tempest detects AR with the inputs of integrated vapor transport (IVT), a metric incorporating water vapor amount and its transport speed. It requires a minimum IVT of 250 kg m^{-1} s^{-1} at a grid cell and minimum cluster size of 120,000 km^2 (Shields et al., 2018). A detailed description of the Tempest-defined AR criteria can be found in Patricola et al. (2020). Note that for the WRF simulations (27 km resolution), we first aggregated its IVT field to match with the coarser grid scale of MERRA2 (~50 km) by area averaging, and then ran the Tempest software to detect simulated ARs. Compared to other AR tracking algorithms, Tempest performs relatively well in capturing the medians of AR statistics range among a large pool of AR tracking algorithms, thus reducing the uncertainty due to the diversity of AR definitions and algorithms (Rutz et al., 2019). Our analysis divides the western US region into three subregions, Oregon and Washington (ORWA), northern California (NCA), and southern California (SCA), facilitating the comparison between landfalling ARs by subregion and overall AR activity across the North Pacific and western half of North America (NPNA; 15°N–55°N and 135°E–100°W in Figure 1). AR frequency is defined as the accumulated number of 6-hourly time steps by grid cell and season, and regional mean AR frequency is calculated by averaging AR frequency across all grid cells within each region.

2.4. Classification of Precipitation Events

To identify daily precipitation events over the western US associated with ARs, we matched landfalling ARs (at least one AR grid point falling within the western US region) and precipitation events based on their timings and locations. The CPC daily observations document 24–h accumulated precipitation ending at 12Z of the day, which are off by half a day when compared to the WRF simulated daily precipitation events (00Z–24Z). Therefore, when we classified daily precipitation events into AR and non-AR categories, the duration of a wet day has to be matched with the time steps of ARs in the same day, avoiding the discrepancy due to inconsistent recording times.

In each 24–h daily interval, we first located all the grid points with ARs in at least one of the five 6-hourly time steps (00Z, 06Z, 12Z, 18Z, and 24Z in the WRF hindcasts; 12Z, 18Z, 24Z, 06Z, and 12Z in CPC). If a grid point records ARs more than once in the same day, then it is only counted once. Next, we searched

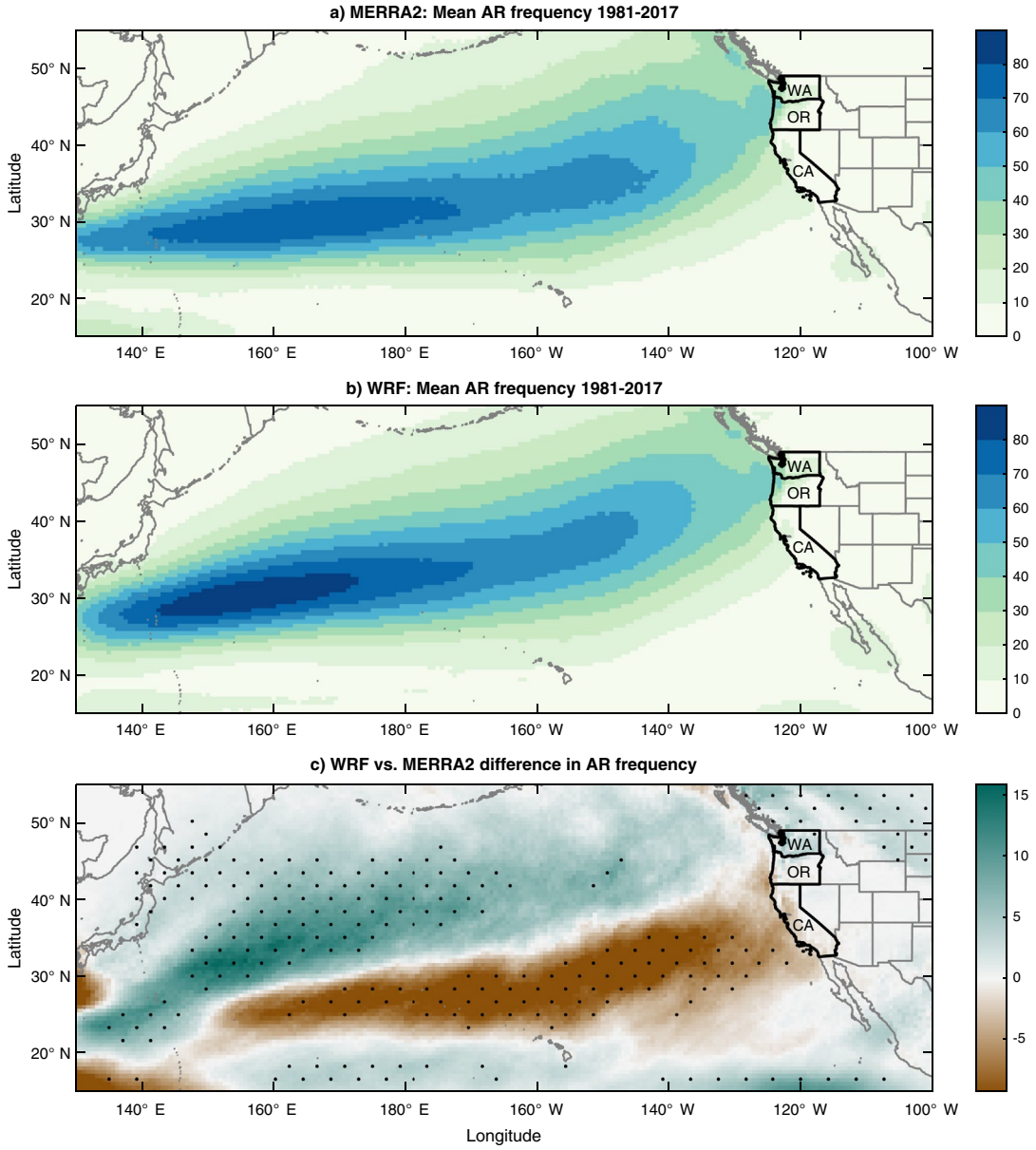

Figure 1. Spatial patterns of winter atmospheric river (AR) frequency (number of 6-hourly time steps per season) in the (a) Modern-Era Retrospective analysis for Research and Applications, Version 2 (MERRA2) reanalysis, (b) Weather Research and Forecast (WRF) hindcasts from 1981 to 2017, and (c) their difference. The spatial map shows the North Pacific and western half of North America (NPNA; 15°N–55°N and 135°E–100°W), which includes the three coastal states of western US, that is, Washington (WA), Oregon (OR), and California (CA). Stippling in (c) refers to a significant difference in AR frequency between WRF and MERRA2 using a grid-cell specific two sample *t*-test with the *p* values adjusted by controlling the false discovery rate (Wilks, 2016) at 0.05.

for grid points that received precipitation within the same 24 h interval. Precipitation events occurring in the AR grid points are counted as AR-induced (AR precipitation), otherwise they are considered non-AR precipitation. The procedures to identify AR precipitation events were also applied by Rutz et al. (2014). We note that the spatial resolutions of the detected AR and precipitation are different, so we aggregated the simulated ARs and precipitation to the MERRA-2 grid (~50 km) using linear interpolation, similar to Huang et al. (2020).

Table 1
Spatially Averaged 1981–2017 Winter Atmospheric River (AR) Frequency, Total Precipitation, AR Precipitation, and AR Contribution to Winter Total Precipitation by Region in the Observations (Modern-Era Retrospective analysis for Research and Applications, Version 2 [MERRA2] for AR Frequency, Climate Prediction Center [CPC] for Precipitation) and Weather Research and Forecast (WRF) Ensemble Mean, Their Relative Difference (%, WRF in Relative to Observations), and Correlation From 1981 to 2017

	NPNA	ORWA	NCA	SCA
AR frequency:				
MERRA2 (time steps season^{-1})	23.6	14.6	8.3	5.6
WRF (time steps season^{-1})	24.6	15.8	7.0	4.6
Difference	+4.1%	+8.1%	−14.7%	−18.7%
Correlation	0.68*	0.64*	0.58*	0.62*
Total precipitation:				
CPC (mm season^{-1})	—	343.3	391.7	141.8
WRF (mm season^{-1})	—	378.4	339.2	81.0
Difference	—	+10.2%	−13.4%	−42.8%
Correlation	—	0.69*	0.62*	0.49*
AR precipitation:				
CPC (mm season^{-1})	—	148.6	144.3	49.1
WRF (mm season^{-1})	—	101.5	62.1	13.1
Difference	—	−31.6%	−56.9%	−73.4%
Correlation	—	0.64*	0.55*	0.23
AR contribution to total precipitation:				
CPC (%)	—	42.2	34.7	32
WRF (%)	—	26.3	16.9	13.2
Difference	—	−37.8%	−51.3%	−58.7%
Correlation	—	0.42*	0.05	0.33*

Note. The asterisk (*) sign indicates that the time series of observations and WRF simulations are significantly correlated at the 0.05 level using two sample *t*-test. The em dash (—) indicates the data is not available or included.

2.5. Climate Mode Indices

The ENSO and MJO are important sources of predicting ARs and precipitation in the western US (DeFlorio et al., 2019; Pan et al., 2019), but their influences on ARs and precipitation remain disputed (see Introduction). The ENSO is the predominant mode of interannual variability of sea surface temperature over the tropical Pacific, which can be represented by different ENSO indices (Capotondi et al., 2015). Here, we used two ENSO indices to explore the influence of ENSO diversity (i.e., different longitude and amplitude of the SST anomalies extrema; Capotondi et al., 2015) on ARs and precipitation. The first index is the traditional Niño 3.4 index, which represents SST anomalies in the central equatorial Pacific (5°S–5°N and 170°W–120°W). The second is the ELI, uniquely characterizing the diversity of ENSO events in a single index of longitude (Williams & Patricola, 2018). The ENSO phases and magnitudes during DJFs 1981–2017 are documented and provided through Table 1 in Patricola et al. (2020). It is worth noting that the identification of ENSO events between the two metrics are slightly different. For example, the Niño 3.4 index indicates that the years with strong El Niño events (≥1.5°C) are 1983, 1992, 1998, 2010, and 2016, however, ELI designates strong El Niño events (≥179°E) in 1983 and 1998. Patricola et al. (2020) found that ELI is better at predicting the western US hydroclimate variability when compared to the Niño 3.4 index, especially during strong El Niño years. Thus, we primarily used the ELI-defined ENSO events in the following analysis, with Niño 3.4-defined ENSO events for comparison. The goal is to evaluate the sensitivity of ENSO-AR relationship to different ENSO indices and facilitate the comparisons with previous studies based on the Niño 3.4 index.

The MJO, an intraseasonal variability with a period of 30–90 days, is characterized by clouds and precipitation anomalies near the equator which moves eastward over the Indian and western-central Pacific oceans (Madden & Julian, 1971, 1972). This feature has global impacts on weather and climate, including ARs and precipitation in the North Pacific and western US (Guan & Waliser, 2015; Zhang, 2005). Here we used the real-time multivariate MJO index calculated from observed outgoing longwave radiation, and 850 hPa and 200 hPa zonal wind (Wheeler & Hendon, 2004), which is available from the Bureau of Meteorology, Australia (http://www.bom.gov.au/climate/mjo/). Eight different MJO phases are defined to mark its propagation across the oceans, and only strong MJO phases (composite amplitude >1) are used to examine their associations with ARs and precipitation. During DJFs 1981–2017, the number of days with strong MJO phases 1–8 is 164, 228, 313, 279, 269, 297, 351, and 244, respectively. We find that the MJO-AR relationship revealed in Figure 8 is not sensitive to the choice of MJO amplitude threshold (not shown). Moreover, earlier studies have shown that regional WRF simulations can reasonably simulate MJO, including the initiation and propagation of MJO events (Fonseca et al., 2019; Hagos & Leung, 2011), cloud characteristics (Hagos et al., 2013, 2015), and the MJO-related variability in precipitation rate (Wang et al., 2016). In the WRF large ensemble domain, we also confirm WRF's capability in simulating MJO events represented by the anomalies in outgoing longwave radiation (not shown). Given that the WRF domain only covers part of the MJO life cycle (Patricola et al., 2020) and the NCEP-DOE AMIP-II global reanalysis provides the initial and boundary conditions for the WRF simulations, we choose to use the real-time multivariate MJO index with the full MJO life cycle to examine the source of hydroclimate predictability.

3. Model Evaluation

This section evaluates the performance of WRF simulations in reproducing the spatial and temporal patterns of observation-based DJF ARs and precipitation. Specifically, landfalling ARs in the three western US subregions are analyzed and compared, besides the overall AR activity in NPNA. AR precipitation and its contribution to DJF total precipitation in the three western US subregions are then assessed.

3.1. Observed and Simulated ARs

In DJF, MERRA2 ARs are most frequently found extending from the northwestern Pacific around 30°N to the Pacific coast of North America (Figure 1a). This pattern resembles the findings by Mundhenk et al. (2016) who used a different AR detection algorithm and older generation of reanalysis product (MERRA). WRF performs adequately well in reproducing the spatial pattern of AR frequency in MERRA2 (Figure 1b) with a pattern correlation of 0.873 (95% confidence interval: 0.871–0.875), in agreement with Patricola et al. (2020). Along the coast of the western US, ORWA experience more frequent ARs than California, which is seen in both the MERRA2 reanalysis and WRF hindcasts. It is notable that WRF overestimates (underestimates) AR frequency in the northwestern (southeastern) North Pacific, but no significant difference is found over the western US (Figure 1c). WRF also performs well in capturing the standard deviation of AR frequency in MERRA2 with a pattern correlation of 0.74 (Figure S3).

Figure 2 shows a large interannual variability in observed landfalling AR frequency but not in NPNA AR activity. From 1981 to 2017, MERRA2 AR frequency in ORWA ranged from 5.4 to 25.2 per season, which is equivalent to 37% and 172% of the 1981–2017 seasonal average (14.6 per season), respectively. In NCA and SCA, the ranges are 17%–241% and 8%–393% of the long-term averages, respectively. In contrast, MERRA2 AR frequency in NPNA ranged between 90.8% and 107.4% of the 1981–2017 average (23.6 per season). The findings suggest that the variability in landfalling AR frequency may be controlled by the large-scale circulation that determines AR location, rather than the AR genesis rate over the ocean basin.

WRF is capable of simulating the climatological mean of AR frequency, as well as its variations over time and space (Figure 2 and Table 1). On average, WRF slightly overestimates the AR frequency in NPNA (+4.1%) and ORWA (+8.1%) but underestimates the AR frequency in NCA (−14.7%) and SCA (−18.7%). The contrasts in simulated AR frequency may be due to a poleward shift in AR landfall locations in the WRF simulations (Figure S2). The variability in WRF ensemble-averaged AR frequency from 1981 to 2017 closely follows MERRA2 and the two time series are significantly correlated in all regions, with the correlation coefficients ranging from 0.58 to 0.64. Each ensemble member in the WRF hindcasts similarly captures the

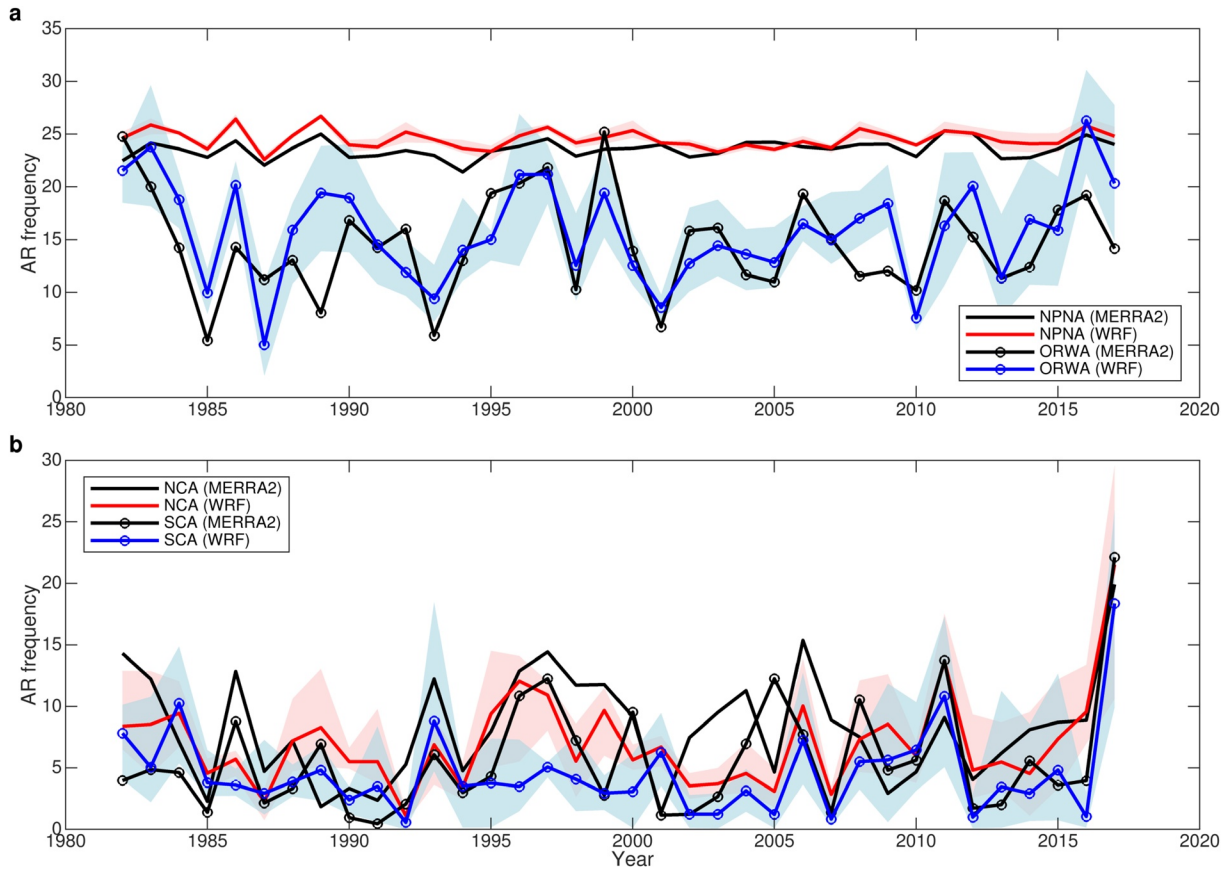

Figure 2. Spatially averaged winter atmospheric river (AR) frequency (number of 6-hourly time steps per season) in the Modern-Era Retrospective analysis for Research and Applications, Version 2 (MERRA2) reanalysis (black lines) and Weather Research and Forecast (WRF) hindcasts (blue and red lines) from 1981 to 2017 over (a) the North Pacific and western half of North America (NPNA), Oregon and Washington (ORWA), and (b) northern California (NCA) and southern California (SCA). These regions are shown in Figure 1. Shadings refer to ensemble spread of AR frequency in the WRF large ensembles, and color lines represent the WRF ensemble means.

variability in MERRA2 AR frequency. For example, the 2016/17 winter marked the strongest AR activity in both NCA and SCA, which is evident across MERRA2 and all WRF ensemble members. Moreover, AR intensity, characterized by average integrated vapor transport, is similar between the MERRA2 and WRF simulations with a 2.2% difference over the western US (Figure S4), further demonstrating WRF's capability in simulating AR activity.

3.2. Observed and Simulated Precipitation

ARs are important contributors to DJF precipitation along the coast of the western US, and the WRF model performs skillfully in simulating the observed spatial patterns of precipitation (including AR precipitation). In the CPC observations, the relatively wet areas in coastal ORWA and NCA largely overlap with the areas affected by active landfalling ARs (Figures 3 and 1), leading to increased AR precipitation (>300 mm season^{-1}) and higher AR contributions (>50%) to DJF total precipitation (Figures 3a–3c). In contrast, the contribution of ARs reduces to less than 20% of total precipitation in the eastern part of western US region. The west-to-east gradient is an indication of the orographic effect of the Cascade Range, which extends from NCA to ORWA and prevents the moist air from the Pacific Ocean from traveling further inland. However, ARs still lead to nearly a third of winter precipitation across the border regions of ORWA due to the lower elevations of the Columbia River basin. The spatial patterns in Figure 3 are in agreement with previous studies (Lavers & Villarini, 2015; Rutz et al., 2014). The WRF simulations can generally reproduce the observation-based gradient of total and AR precipitation, and therefore the AR contribution to seasonal total precipitation (Figures 3d–3f), despite a smaller amplitude. Another analysis based on the PRISM gridded

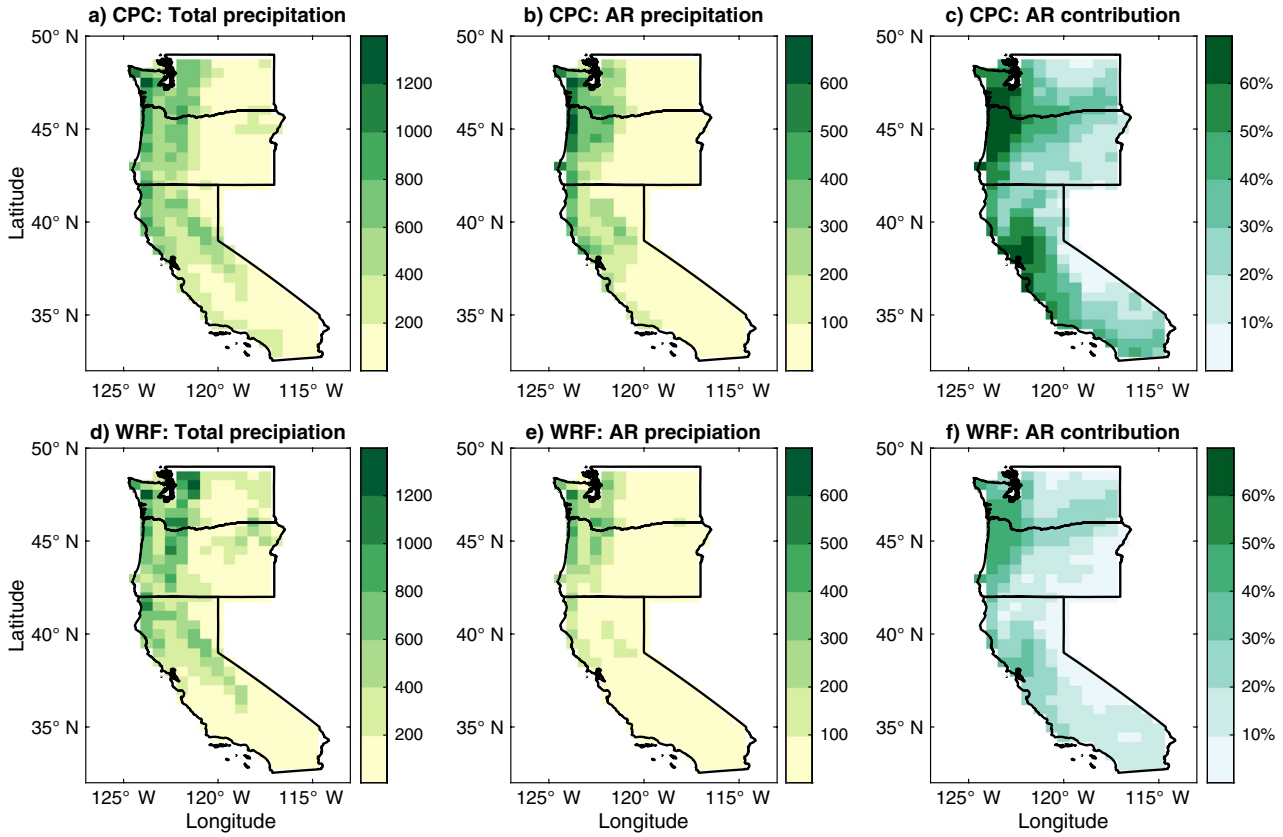

Figure 3. Spatial patterns of 1981–2017 winter total precipitation (mm season^{-1}), atmospheric river (AR) associated precipitation (mm season^{-1}), and the relative contribution of ARs to total precipitation in the Climate Prediction Center (CPC) observations (a–c) and Weather Research and Forecast (WRF) hindcasts (d–f).

observations (as opposed to the CPC observations) reveals similar precipitation patterns between observations and the WRF simulations (Figure S5). The findings are supported by Patricola et al. (2020) and Leung and Qian (2009) who found similar patterns of WRF-simulated winter precipitation over the western US as observations. The dry bias in WRF-simulated AR precipitation, also found by Martin et al. (2018), is linked to the underestimation of AR frequency in California and Oregon (Figure S2), rather than AR intensity (Figure S4). Another possible cause is model limitation in capturing the physical processes (e.g., cloud microphysics, surface energy fluxes) critical to the development of AR precipitation events (Gershunov et al., 2019; Martin et al., 2018). It is found that increasing model resolution made a little difference in simulated AR precipitation (Kim et al., 2018). Developing more accurate model forcing data (especially low-level jet water vapor flux) and physics parameterizations of subgrid-scale processes (e.g., surface energy fluxes and cloud microphysics) may lead to more skillful simulation of AR precipitation (Martin et al., 2018). Therefore, future work is needed to evaluate the performance of WRF in simulating AR precipitation with state-of-the-art cloud microphysics schemes and forcing data (such as ERA5 reanalysis), though it is not within the scope of the current study.

The WRF model also performs well in simulating the observation-based temporal variability of DJF total precipitation and AR precipitation, despite an underestimation of precipitation amount (Table 1; Figures 4 and S6). For total precipitation, the differences between the WRF simulations and CPC observations are +10.2%, −13.4%, and −42.8% in ORWA, NCA, and SCA, respectively. Significant correlations are found between the two time series across all three regions ($p < 0.01$; Table 1). In the CPC observations, 148.6 mm (42.2%), 144.3 mm (34.7%), and 49.1 mm (32%) of seasonal total precipitation are associated with ARs in ORWA, NCA, and SCA, respectively (Table 1). In the WRF simulations, regional averages of AR precipitation are much lower when compared to the CPC observations, but the time series of AR precipitation are still significantly correlated with the observations in ORWA and NCA ($p < 0.001$). In SCA, the correlation

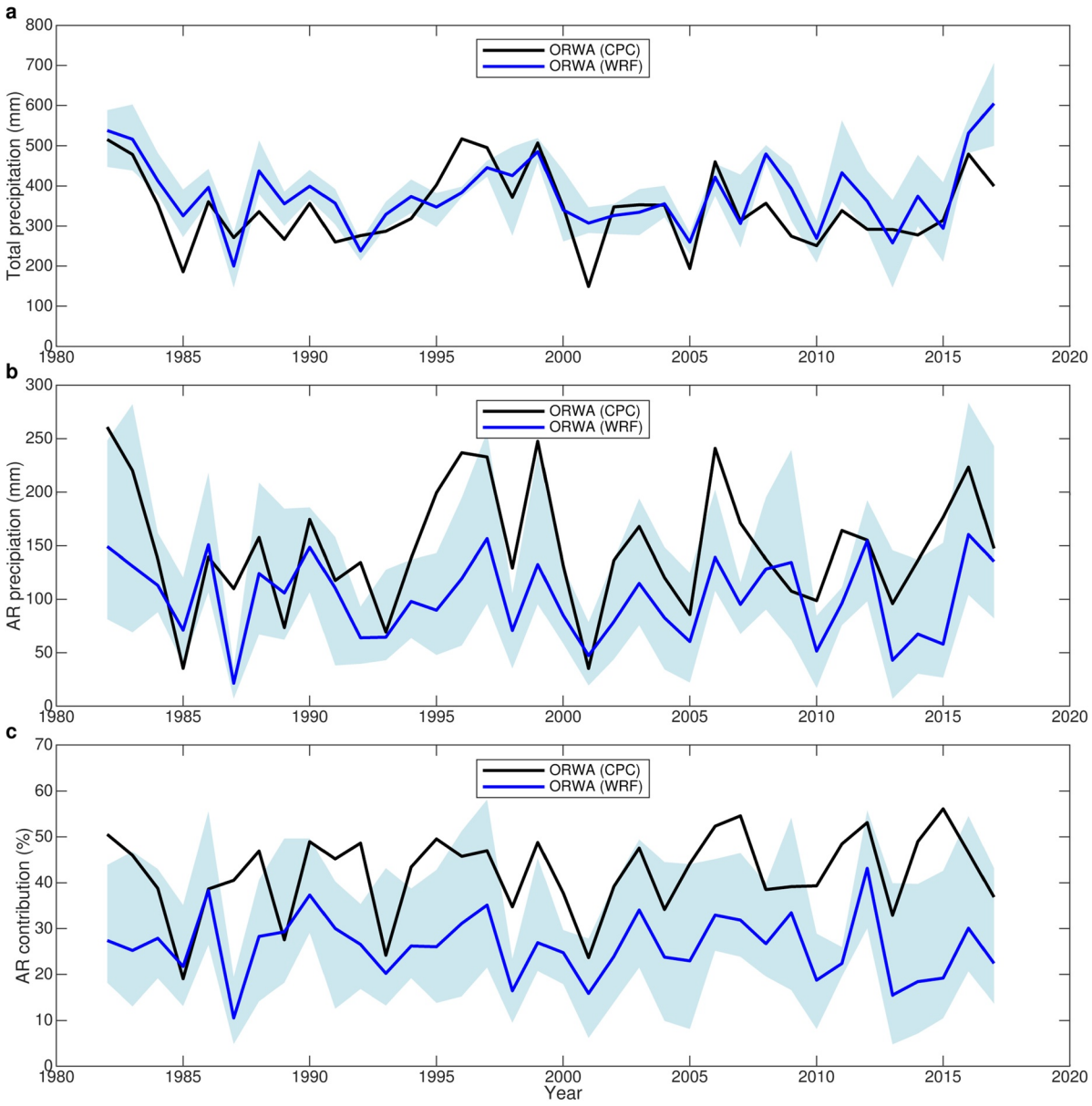

Figure 4. Spatially averaged 1981–2017 winter total precipitation (a), atmospheric river (AR) associated precipitation (b), and the relative contribution of ARs to total precipitation (c) in the Climate Prediction Center (CPC) observations (blue lines) over Oregon and Washington (ORWA). Blue shadings refer to ensemble spread in the Weather Research and Forecast (WRF) hindcasts, and blue lines represent the WRF ensemble means.

is weaker and insignificant ($r = 0.23$, $p = 0.18$). Not surprisingly, there exist large biases in the relative contributions of ARs to total precipitation across all three regions, but positive and significant correlations ($p < 0.05$) between the observed and simulated AR contributions are found in ORWA and SCA. The underestimations of AR precipitation in NCA and SCA are largely attributed to WRF's underestimations of landfalling AR frequency (Figures 2 and S2). In ORWA, simulated AR precipitation is 31.6% lower than that of the observations, even with 8.1% higher AR frequency and 10.2% higher total precipitation. This further demonstrates WRF model's limitation in simulating AR precipitation events.

AR precipitation is positively correlated with seasonal total precipitation (r: 0.54–0.87) in all regions, consistently seen in the observations and WRF simulations. This highlights the vital role of landfalling AR activity in contributing to seasonal total precipitation. In contrast, there is generally a weak and insignificant correlation between AR frequency in NPNA and AR precipitation in any of the western US subregion

(except simulated AR and precipitation in ORWA), implying that overall AR activity in NPNA may not be a useful predictor of precipitation in the western US. For example, in DJF 2016/17, observed total precipitation (AR precipitation) doubled (tripled) in both NCA and SCA, which were caused by 2.4 and 3.9 times more frequent landfalling AR activity, respectively. However, AR frequency over NPNA is virtually the same as the climatological mean over the same season. The AR-precipitation relationship is similarly reproduced in the WRF hindcasts. What physical mechanisms lead to the weak connection between NPNA AR frequency and western US precipitation is beyond the scope of this study, but warrants future research.

4. Results and Discussion

To evaluate the sources of subseasonal-to-seasonal predictability of ARs and precipitation, we first examine the effect of different ENSO events on seasonal NPNA and landfalling ARs, as well as AR-related precipitation in the western US. Then we investigate the influence of MJO phases on subseasonal ARs and associated precipitation. Lastly, the joint influences of ENSO and MJO on ARs and precipitation are assessed. Both the observations and WRF large ensembles are utilized to explore the relationship between the climate modes (ENSO and MJO) and western US hydroclimate.

4.1. The Effect of ENSO on ARs and Precipitation

In this section, we primarily use the ELI-defined ENSO events in the following analysis, but also explore Niño 3.4-defined ENSO events for comparison, as discussed in Section 2.5. We compare the results from the WRF simulated ARs and precipitation to those from observation-based ARs and precipitation by ENSO phase. We show the resulting figures from the WRF-derived analysis in this section, and observation-based figures in the supplement for the purpose of comparison. It is worth noting that the number of years (36 water years in total from 1981 to 2017) and El Niño/La Niña events are very limited in the MERRA2 and CPC observations, making a robust and physically based comparison of ARs and precipitation between ENSO phases difficult when compared to those in the WRF hindcasts (318 model years in total from 1981 to 2017).

We find the ELI-based ENSO events have distinct effects on AR activity at ocean basin and regional scale over the North Pacific (Figure 5). ENSO events have minor effects on basin-wide averaged AR activity, as shown by the small interannual variability in NPNA AR frequency (Figure 2) and similar distributions of ARs track density during different ENSO phases (not shown) as in Figure 1. At regional scale, ENSO events substantially modulate simulated ARs across NPNA (Figure 5). Specifically, AR activity is strengthened along 30°N and weakened to its south and north during El Niño years. Despite some regional differences between La Niña and ENSO neutral years, AR activity is weakened along 30°N and strengthened to the south and north, which contrasts with El Niño years. Similar responses with the three ENSO phases are also evident in the MERRA2 AR spatial patterns (Figure S7), as well as the MERRA2 and WRF-simulated AR patterns based on the Niño 3.4-defined ENSO events (not shown). The patterns, consistent with Mundhenk et al. (2016) and Kim et al. (2017), are associated with an enhanced (weakened) Aleutian Low and equatorward (poleward) shifted subtropical jet during El Niño (La Niña) years (Kim et al., 2017; Payne & Magnusdottir, 2014).

In the western US, ENSO events exert different influences on AR activity at grid point and regional scale (Figure 5). Over a large majority of grid points in the western US, AR frequencies are not significantly different between any one of the three ENSO phases and the climatological mean, consistent with Guan and Waliser (2015) and Mundhenk et al. (2016). When aggregating over the western US region, we find below-average (above-average) AR frequency relative to DJF climatology during ELI-based El Niño (La Niña) periods in both the WRF simulations and MERRA2 reanalysis (Figures 5, S7–S9). In contrast, when ENSO events are defined by the traditional Niño 3.4 index, above-average (below-average) AR frequency in the MERRA2 reanalysis is found during El Niño (La Niña) events, though their differences from climatology are small (Figure S10). The latter is in qualitative agreement with Payne et al. (2014), Mundhenk et al. (2016), and Kim et al. (2017) whose conclusions were also based on traditional ENSO indices defined by SST anomalies over a fixed region. The agreement among studies and disagreement between ENSO indices imply that ENSO diversity can alter the empirical relationship between ENSO and landfalling AR activity, thus leading to large uncertainties.

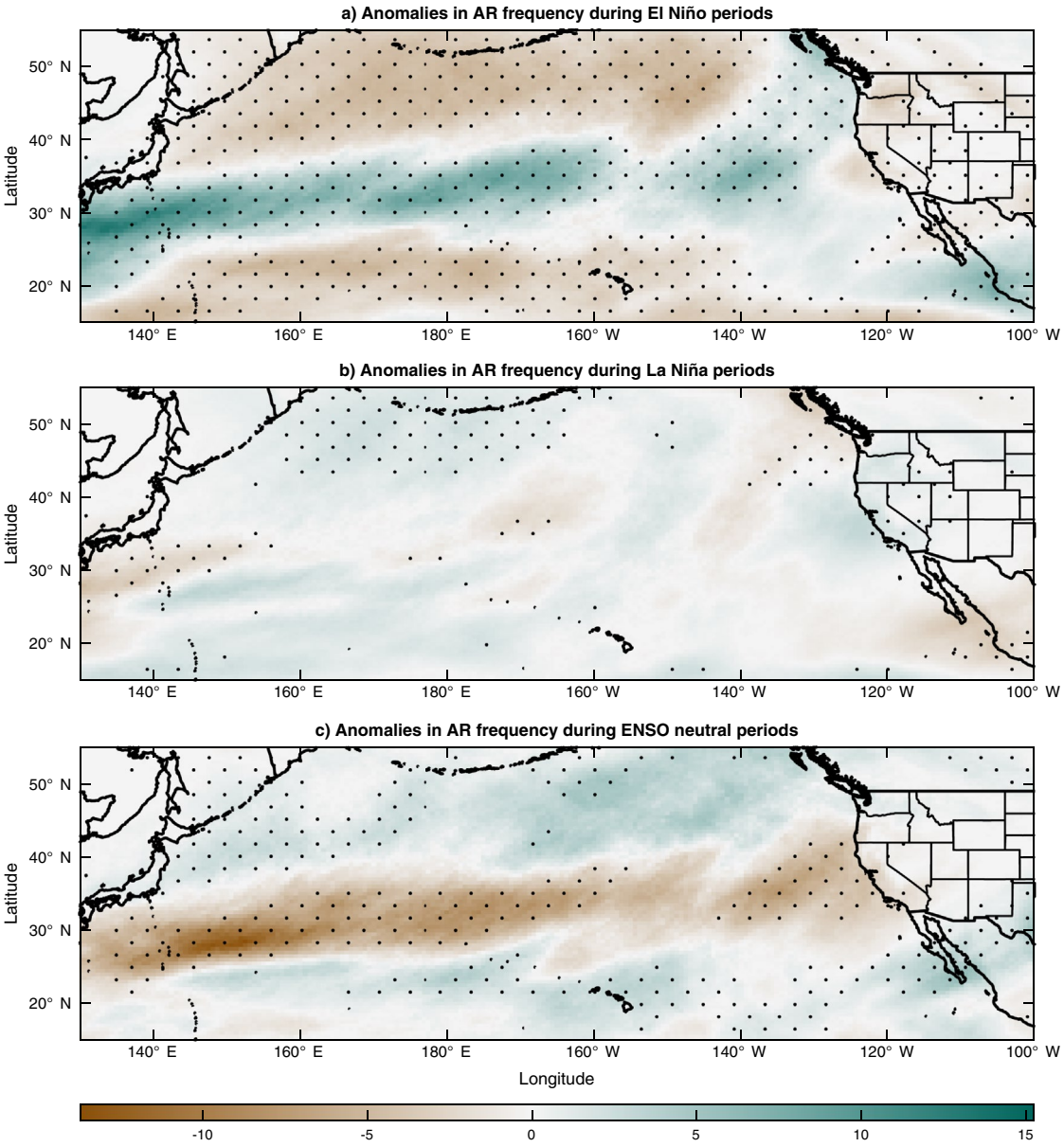

Figure 5. Spatial patterns of anomalies in the Weather Research and Forecast (WRF) model-simulated atmospheric river (AR) frequency (number of time steps season^{-1} in relative to winter climatology) during the El Niño/Southern Oscillation (ENSO) Longitude Index (ELI)-based (a) El Niño, (b) La Niña, and (c) ENSO neutral phases. The western US region is shown with finer details in Figure S8. Stippling refers to a significant difference in AR frequency between individual ENSO phase and climatology using a grid-cell specific two-sample t test with the *p* values adjusted by controlling the false discovery rate at 0.05.

For the WRF-simulated ARs in the western US, we find significantly higher AR activity ($p < 0.05$) in the Niño 3.4-defined La Niña years than El Niño and ENSO neutral years (Figure S11). This is inconsistent with the MERRA2-based ENSO–AR relationship, despite the same algorithm (Tempest) is used to detect ARs. This is due to a large underestimation (−19.2% in relative to MERRA2) of AR frequency by WRF during central Pacific El Niño periods, as compared to an underestimation of 4.4% during eastern Pacific El Niño events. The WRF-based ENSO-AR correlation is also contrary to the findings in Payne et al. (2014) and Kim et al. (2017). A further analysis reveals that with eastern Pacific El Niño events as defined by the Niño 3 index (i.e., 1982/83, 1991/92, 1997/98, 2015/16, equivalent to strong and moderate El Niño events based on ELI), above-normal AR activity is found in both MERRA2 and WRF data (Figures 2 and 6), consistent with Kim et al. (2017). As demonstrated by Patricola et al. (2020; see Figure 12 therein) and Figure 6, more frequent landfalling AR activity in the WRF simulations is generally found during extreme El Niño years

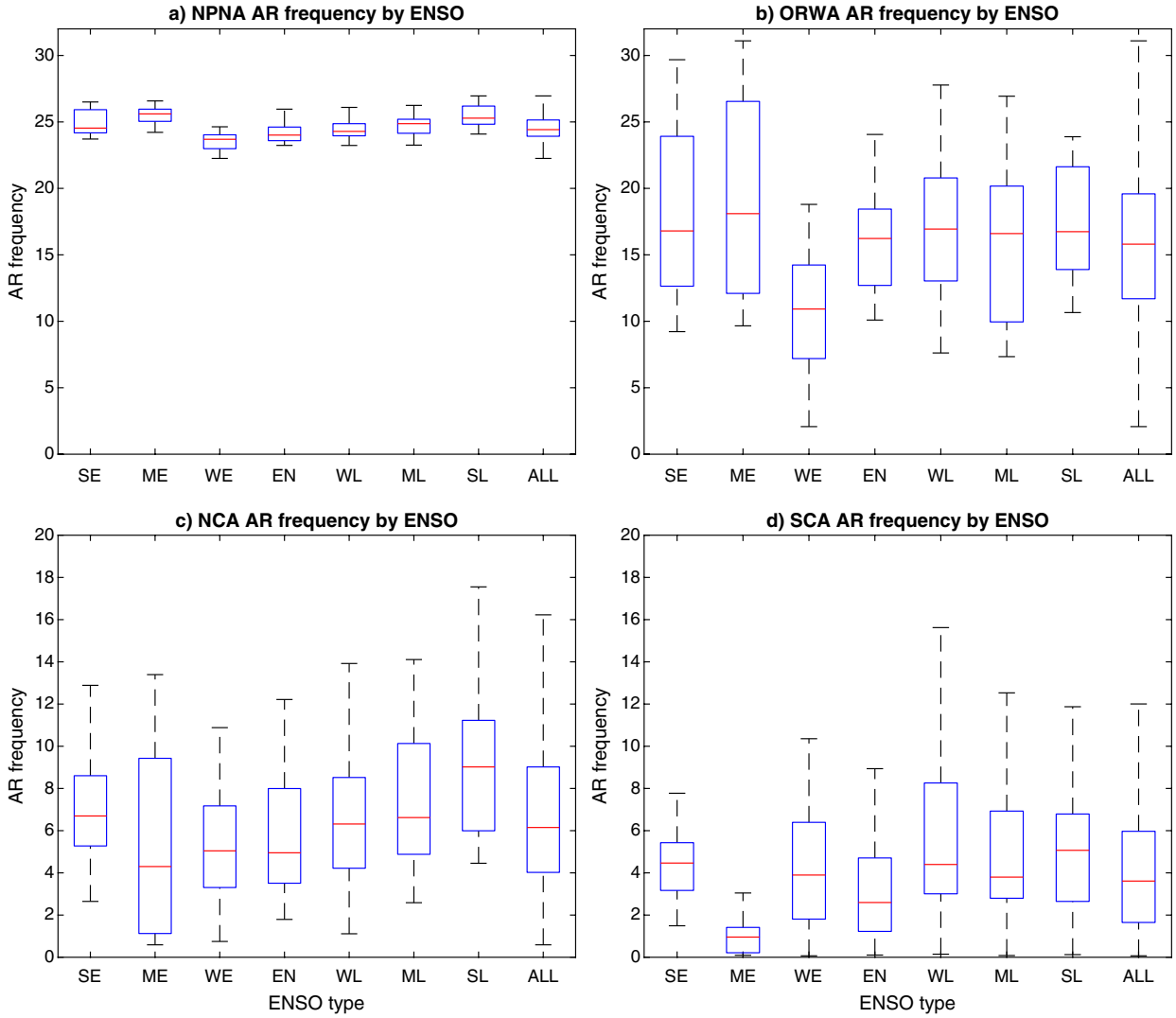

Figure 6. Boxplots of the Weather Research and Forecast (WRF) model-simulated atmospheric river (AR) frequency by region and the El Niño/Southern Oscillation (ENSO) Longitude Index (ELI)-based ENSO type from winters 1981–2017 over (a) the North Pacific and western half of North America (NPNA), (b) Oregon and Washington (ORWA), (c) northern California (NCA), and (d) southern California (SCA). Different types of ENSO events (and abbreviations) include strong El Niño (SE), moderate El Niño (ME), weak El Niño (WE), ENSO neutral (EN), weak La Niña (WL), moderate La Niña (ML), strong La Niña (SL), and all events combined (ALL). To ensure an equal weighting of simulated ARs by year, the years with five ensemble members are duplicated five times to make them 25-member ensemble years. Due to large number of outliers, they are excluded in these plots for improved visualizations of boxes.

(except 1991/92 with weaker AR activity). With central Pacific El Niño events as defined by the Niño 4 index (i.e., 1994/95, 2002/03, 2004/05, 2009/10, equivalent to weak El Niño events based on ELI), we uncover below-normal landfalling AR activity in both the MERRA2 reanalysis and WRF simulations (Figures 2 and 6), inconsistent with Kim et al. (2017).

The inconsistency may be due to choice of AR definition and detection algorithm, with the Tempest tracking algorithm in the current study being more restrictive than the ones used in Payne et al. (2014) and Kim et al. (2017). Rutz et al. (2019) concluded that AR tracking methods with more restrictive criteria usually detect less frequent ARs, consistent with our findings. Given the small and insignificant difference in MERRA2 landfalling AR frequency between El Niño and La Niña periods, it is of importance to examine whether the detected ENSO-AR relationship is sensitive to tracking algorithms other than Tempest. The Tier 1 experiment in the Atmospheric River Tracking Method Intercomparison Project (ARTMIP; Rutz et al., 2019) provides a unique resource to test the hypothesis, though it is beyond the scope of the current study. Zhou et al. (2020) did examine the uncertainty of ENSO-AR relationship stemming from eight global

AR tracking algorithms participating in the ARTMIP Tier 1 experiment. They showed that while all algorithms consistently capture the changes of AR by ENSO over the North Pacific basin, uncertainty is large for landfalling AR frequency because of its sensitivity to the design of algorithms (i.e., AR detection thresholds). To sum up, the ENSO-AR relationship depends on ENSO indices and climate datasets (and possibly AR detection algorithms as well), with the ELI identifying enhanced landfalling AR activity during extreme (or eastern Pacific) El Niño events. The findings highlight ELI as a valuable source of seasonal predictability of landfalling ARs, besides precipitation in the western US (Patricola et al., 2020).

Next, we further examine the characteristics of AR frequency with strong, moderate, and weak El Niño/La Niña phases, and the ENSO neutral phase (Figure 6). Similar changes in AR activity are found in NPNA and ORWA, characterized by significantly less frequent ARs with weak El Niño phase and more frequent ARs with moderate El Niño and strong La Niña phases. In California (including NCA and SCA), stronger AR activity is linked to La Niña and strong El Niño phases, while weaker AR activity is tied to moderate El Niño and ENSO neutral phases. This echoes the contracts in landfalling ARs between La Niña phase and El Niño and ENSO neutral phases (Figure 5). We also explore the ENSO-AR relationship using the traditional Niño 3.4 index and find similar results as the ELI, except for ARs with moderate El Niño phase in NPNA and ORWA (Figure S11).

The amount of precipitation associated with landfalling ARs (AR precipitation) corresponds well with AR frequency by ENSO phase (Figure 7). Specifically, in ORWA, El Niño phase has less AR precipitation than La Niña phase ($p < 0.001$), primarily because weak El Niño phase is associated with significantly less AR precipitation than the other ENSO phases. In NCA and SCA, moderate El Niño and ENSO neutral phases are characterized by less AR precipitation. In NCA, El Niño phase has significantly less AR precipitation than La Niña phase ($p < 0.001$), but the difference is insignificant in SCA ($p = 0.11$). The ENSO-AR precipitation relationship is a response to the ENSO-AR frequency connection, as also found by Kim et al. (2017) and Guan and Waliser (2015), because the intensities of AR precipitation events in El Niño and La Niña phases are similar (Payne & Magnusdottir, 2014). Furthermore, the percentage contribution of ARs to seasonal total precipitation generally aligns with the amount of AR precipitation in NCA and SCA (Figures 7e, 7f and 7b–7c). However, this is not the case in ORWA due to precipitation events induced by non-AR meteorological systems (e.g., extratropical cyclones, monsoon) and their responses to different ENSO phases (Sellars et al., 2015).

4.2. The Effect of MJO on ARs and Precipitation

Figure 8 exhibits the anomalies in DJF landfalling AR frequency (relative to DJF climatology) following the MJO phases with a time lag of 0–36 days. The time lags are chosen because the MJO phases exert influence on AR activity (especially those making landfall) at downstream longitudes of the MJO convection and the process usually takes days to weeks (Jin & Hoskins, 1995; Mundhenk et al., 2018). In ORWA, MERRA2 AR frequency in DJF is below seasonal average for up to 2 weeks after the occurrence of MJO phase 1, above-average during the third week, and below-average again in week four and five (Figure 8a). AR frequency following MJO phase 2 echoes the evolution of AR anomalies with phase 1, except for shorter time lags, which is expected with the typically sequential occurrences of phases 1 and 2. From phases 3 to 5, ARs are higher than normal within the first week of time lag. The similarity in AR frequency anomalies along the diagonal (from long to short time lags; Figure 8a) suggests a linkage between MJO and landfalling AR activity.

WRF simulations generally agree with the MERRA2 AR-MJO relationship in ORWA, such as the overall lower AR frequency following MJO phases 1–2 and 7–8 and higher AR frequency for two weeks subsequent to phases 3–5 (Figure 8d). The sign agreement in AR anomalies (anomalies are both positive or negative) between MERRA2 and WRF is found in 65.1% of MJO-time lag periods, with 23% of being positive and 42.1% negative (Figure 9a), and the magnitudes of anomalies vary by MJO-time lag period (Figures 8a and 8d). The remaining 34.9% shows disagreement between the two datasets. Within the 36-day lag time period, the percentage of agreement in AR anomalies is 53.1% for 14 lagged days and longer and 85.7% for under 14 days. The evidence demonstrates that WRF is skillful in simulating relative changes in AR frequency associated with MJO phases.

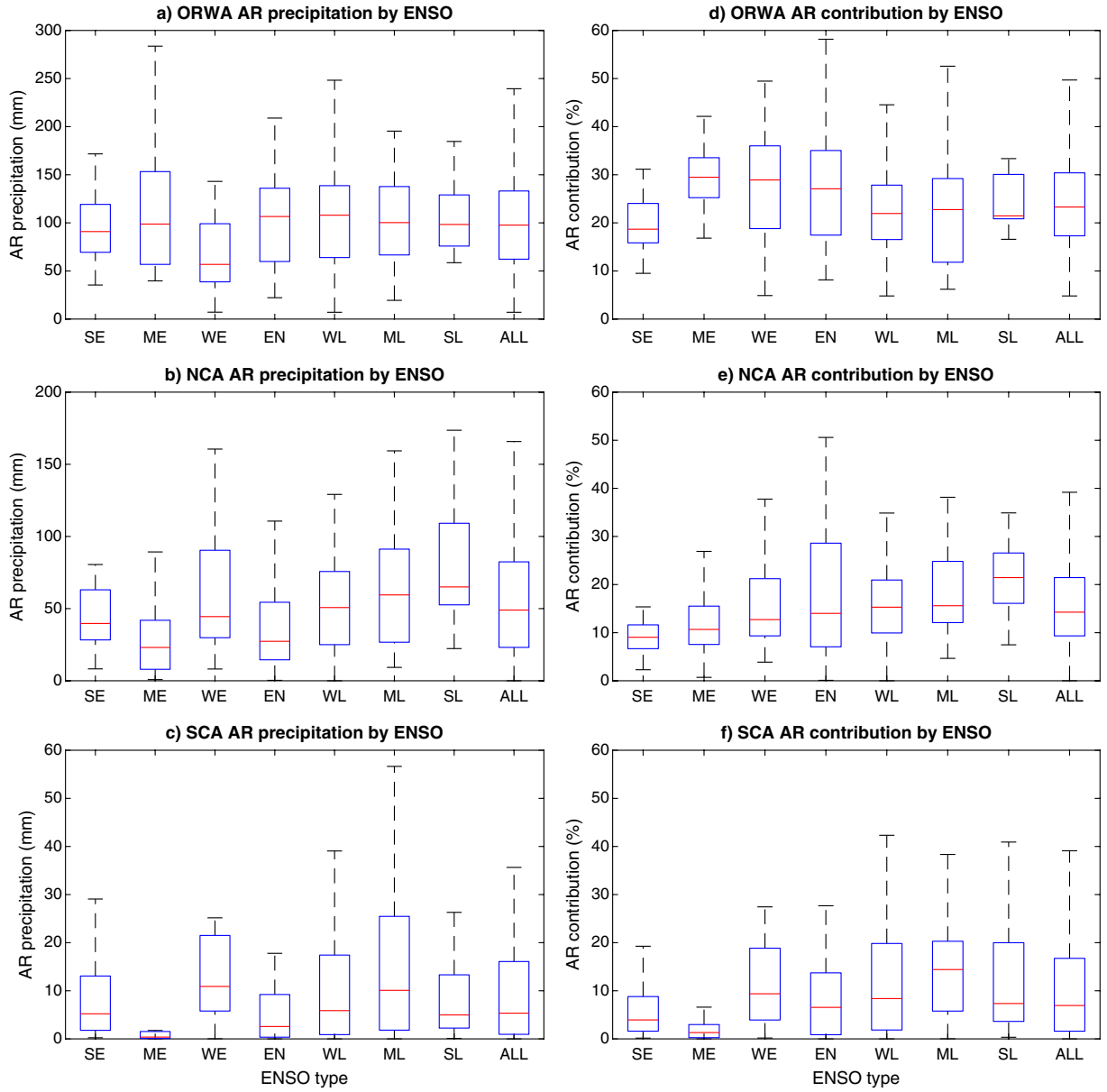

Figure 7. Boxplots of the Weather Research and Forecast (WRF) model-simulated atmospheric river (AR) precipitation (a), (b), and (c) and their relative contributions to total precipitation (d), (e), and (f) by region and the El Niño/Southern Oscillation (ENSO) Longitude Index (ELI)-based ENSO type from winters 1981–2017 over Oregon and Washington (ORWA), northern California (NCA), and southern California (SCA). To ensure an equal weighting of simulated ARs by year, the years with five ensemble members are duplicated five times to make them 25-member ensemble years. Different types of ENSO events (and abbreviations) include strong El Niño (SE), moderate El Niño (ME), weak El Niño (WE), ENSO neutral (EN), weak La Niña (WL), moderate La Niña (ML), and strong La Niña (SL).

In NCA, MERRA2 AR frequency tends to be lower than the seasonal average in the 2–4 weeks succeeding MJO phases 2–3, but increases to above-average in the fifth week subsequent to phases 4–5 (Figure 8b). In SCA, similar anomalies in MERRA2 AR frequency are found along the diagonal (from long to short time lags), as shown in Figure 8c. The signs of WRF-simulated AR anomalies agree with MERRA2 AR anomalies in 48.7% and 59.9% of MJO–time lag periods in NCA and SCA, respectively (Figures 9b and 9c), despite varying magnitudes of anomalies (Figures 8e and 8f). Additionally, in both NCA and SCA, the percentages of agreement (WRF vs. MERRA) for longer and shorter than 14 lagged days are virtually the same. The MJO-AR relationships in ORWA, NCA, and SCA are in good agreement with those reported by Mundhenk et al. (2018; Figures 2 and S2 therein). Moreover, increased landfalling ARs were found during MJO phase

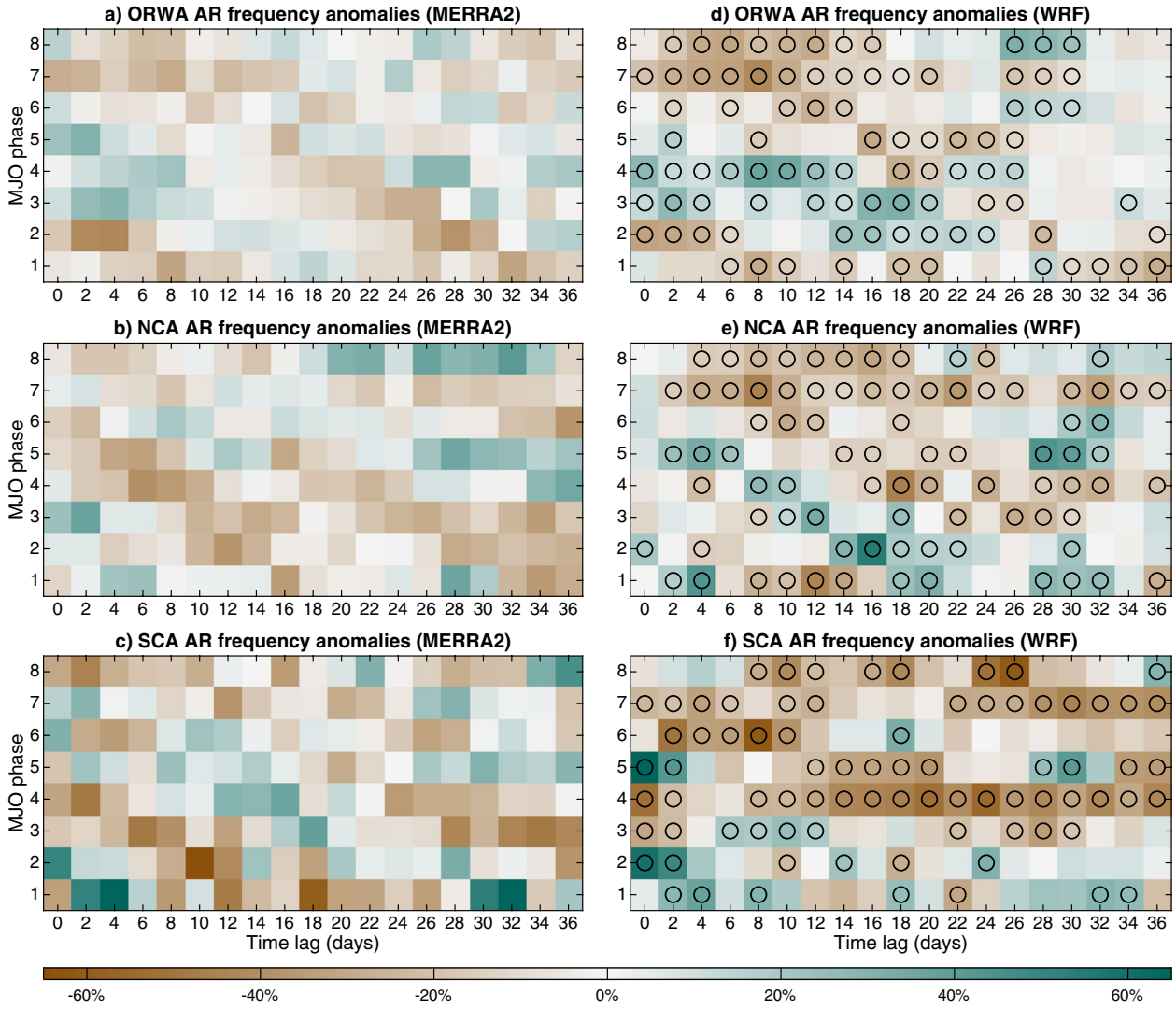

Figure 8. Modern-Era Retrospective analysis for Research and Applications, Version 2 (MERRA2) (a–c) and Weather Research and Forecast (WRF) model simulated (d–f) anomalies in atmospheric river (AR) frequency (percentage difference in relative to all days in winter) by region and Madden-Julian oscillation (MJO) phase over (a, d) Oregon and Washington (ORWA), (b, e) northern California (NCA), and (c, f) southern California (SCA). There are 36 water years (1981–2017) in the MERRA2 reanalysis and 318 model years from 1981 to 2017 in the large ensemble WRF simulations. Circle refers to a significant difference in AR frequency between respective MJO lag days and all winter days using two sample *t*-test with the *p* values adjusted by controlling the false discovery rate at 0.05.

6 when tropical convection is strong in the western Pacific (Guan & Waliser, 2015; Guan et al., 2012; Payne & Magnusdottir, 2014), consistent with the observed and simulated AR activity without time lag in the western US (except NCA ARs in MERRA2 and SCA ARs in WRF). The connections between MJO and land-falling ARs may inform future predictions of ARs in the western US.

We note that after accounting for the multiplicity in testing following Wilks (2016), no significant difference in MERRA2 AR frequency between any MJO phase and seasonal climatology (i.e., all winter days) is found, but significant differences in WRF simulated AR frequency are found over half of MJO and time lags (Figure 8). The inconsistency is related to the small sample size in MERRA2 (36 water years from 1981 to 2017) and large sample size in WRF (318 model years from 1981 to 2017). If we randomly select a single WRF realization from each year to form a new 36-year period (i.e., 1981–2017) to mimic the MERRA2 AR time series, rather than using the large ensemble, the strong signals in the full WRF hindcasts do not exist.

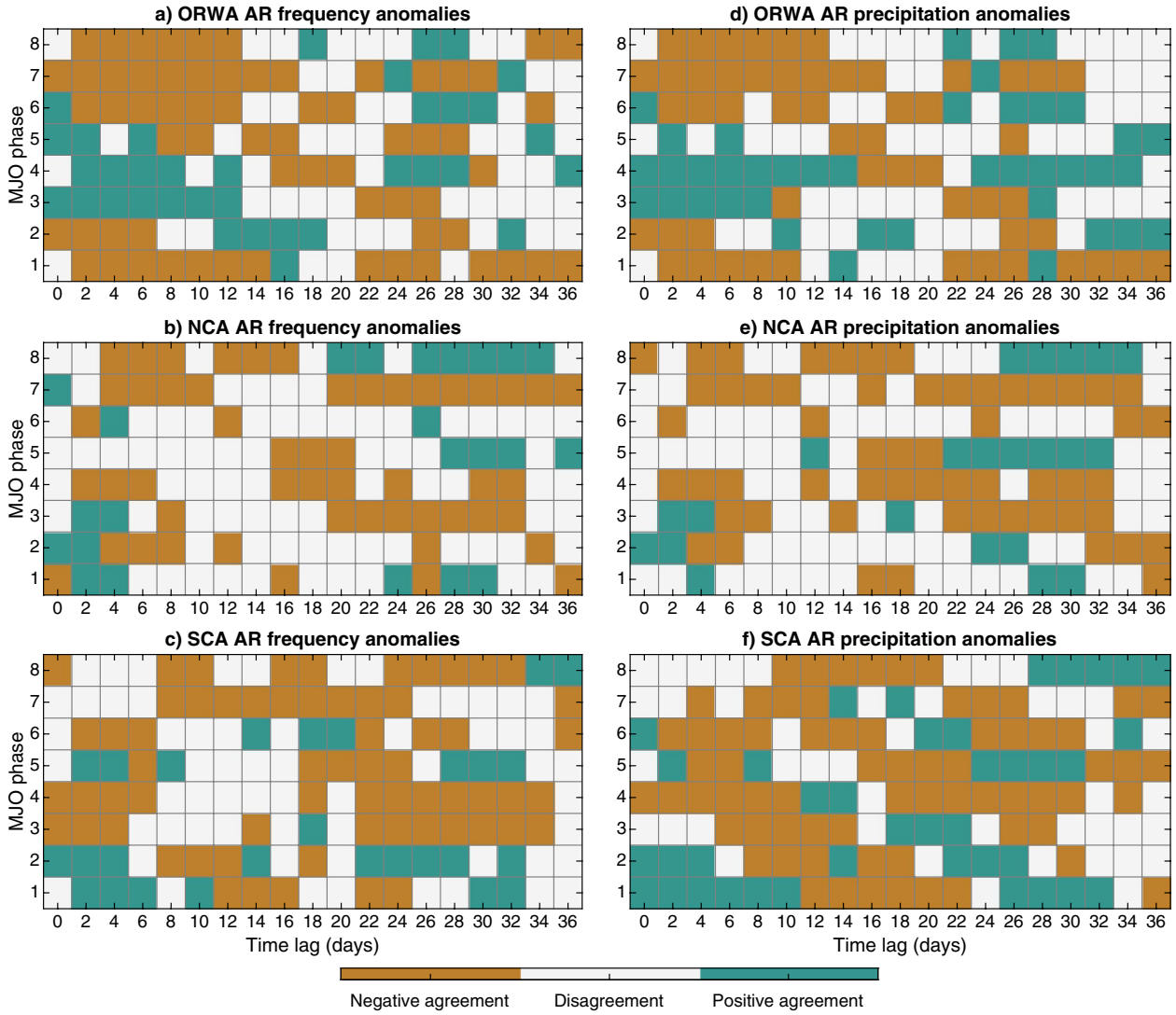

Figure 9. Agreement and disagreement in atmospheric river (AR) frequency (a–c) and AR precipitation (d–f) anomalies between observation-based data and the Weather Research and Forecast (WRF) model simulations by region and Madden-Julian Oscillation (MJO) phase over (a, d) Oregon and Washington (ORWA), (b, e) northern California (NCA), and (c, f) southern California (SCA). Positive agreement (anomalies are both positive) and negative agreement (anomalies are both negative) are highlighted with green and orange colors, respectively, and disagreement in anomalies is represented by white color.

Figures 10 and 9d–9f show that the anomalies in AR precipitation align with the anomalies in AR frequency during most of MJO-time lag periods. For example, both the CPC observations and WRF simulations agree that the first week after MJO phase 1 (3) is characterized by decreased (increased) AR precipitation in ORWA, which is a result of weakened (enhanced) AR activity. Considering the strong and significant correlations between DJF AR frequency and precipitation (including AR precipitation and total precipitation; Figure 4), MJO can serve as an important source of predicting precipitation. We find the largest increase in observed AR precipitation during MJO phase 3 (time lag 0) in the western US, similar to Payne and Magnusdottir (2014). AR precipitation during MJO phase 6 is not significantly higher than other phases (except simulated precipitation in SCA), which is also reported by Guan and Waliser (2015) and Payne and Magnusdottir (2014). As with AR frequency, significant differences in AR precipitation among different MJO phases are not found after considering false discovery rate and the effect of sample size.

In ORWA, the qualitative agreement in AR precipitation anomalies between CPC and WRF is found in 61.8% of MJO-time lag periods, including 27% of positive and 34.9% of negative agreements (Figure 9d),

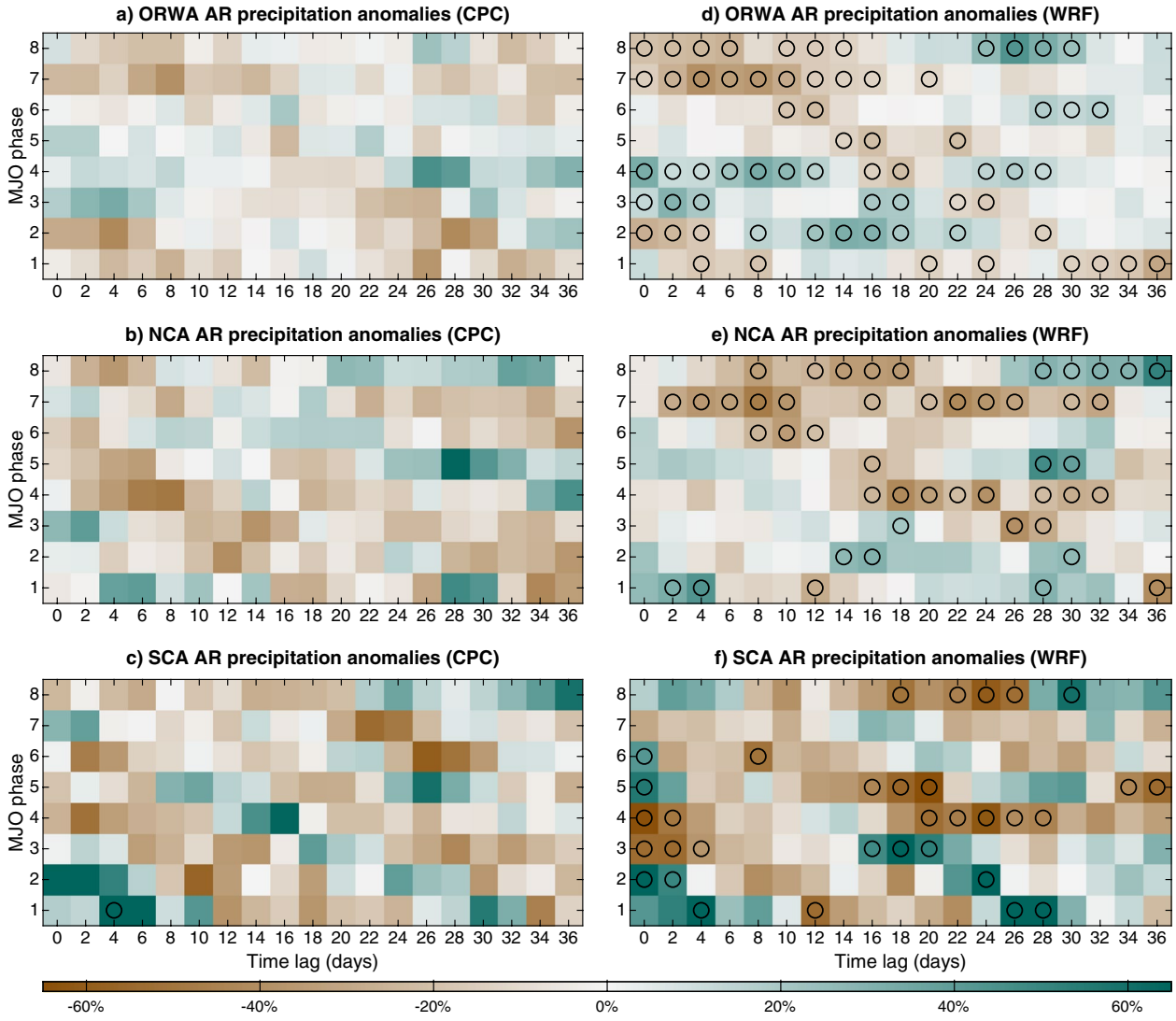

Figure 10. Climate Prediction Center (CPC) observational (a–c) and Weather Research and Forecast (WRF) model simulated (d–f) anomalies in atmospheric river (AR) precipitation (percentage difference in relative to all days in winter) by region and Madden-Julian oscillation (MJO) phase over (a, d) Oregon and Washington (ORWA), (b, e) northern California (NCA), and (c, f) southern California (SCA). There are 36 water years (1981–2017) in the Modern-Era Retrospective analysis for Research and Applications, Version 2 (MERRA2) reanalysis and 318 model years from 1981 to 2017 in the large ensemble WRF simulations. Circle refers to a significant difference in AR precipitation between respective MJO lag days and all winter days using two sample *t*-test with the *p* values adjusted by controlling the false discovery rate at 0.05.

which is similar to the degree of agreement in AR frequency. In NCA and SCA, the qualitative agreement exists over a majority of time periods (NCA: 52%, including 14.5% positive and 37.5% negative; SCA: 71%, including 25.7% positive and 45.4% negative), as shown in Figures 9e and 9f. Within the 36-day lag time period, the percentages of agreement in AR precipitation for longer and shorter than 14 lagged days are similar to those in AR frequency over all three regions.

The anomalies in AR and precipitation over the western US are supported by earlier studies which explored the modulation of MJO on atmospheric dynamics. Gibson et al. (2020) reported that MJO events can modulate ridging over the western US and therefore AR and precipitation anomalies. In particular, the west-ridge type (a positive geopotential height anomaly centered offshore from California) generally leads to reduced AR and precipitation in California, and the ridge's frequency increased significantly after MJO phases 3–6 with a time lag of 2–4 weeks. Its associated AR and precipitation deficits are consistent with our findings. Henderson et al. (2016) found a significant decrease (increase) in blocking frequency averaged between

40°N and 60°N over the East Pacific in the two weeks following MJO Phase 3 (7). The anomaly may result in increased (decreased) AR and precipitation over the western US (Figures 8–10).

4.3. The Concurrent Effects of ENSO and MJO on ARs and Precipitation

Landfalling ARs are not only subject to the individual effects of ENSO and MJO, but also influenced by their combined effects. Figure S12 exhibits the responses of MERRA2 AR frequency to strong MJO phases (amplitude >1) during El Niño and La Niña winters, respectively. In ORWA, only 54% of El Niño-MJO and La Niña-MJO conditions agree with the same sign of anomalies in AR frequency (relative to DJF climatology). For example, in the first week following MJO phase 2 (4), decreased (increased) AR activity is accompanied with both El Niño and La Niña phases, but discrepancies exist in MJO Phase 1 with time lags of 0, 2, and 4 days (Figure S12a and S12d). In NCA and SCA, the percentage of agreements between El Niño-MJO and La Niña-MJO conditions are 50% and 44.7%, respectively (Figures S12b, S12e, S12c and S12f). In the first one to two weeks following MJO phases 1–3, AR activity in NCA is increased under El Niño conditions, whereas it is generally decreased with La Niña conditions (Figure S12b and S12e). The contrasting responses lead to modest changes in AR activity when examining the combined effects of ENSO events (Figure 8b). For AR precipitation, similar percentages of AR agreement between El Niño-MJO and La Niña-MJO conditions are found in ORWA (57.9%), NCA (54.6%), and SCA (51.3%), as shown in Figure S13. The findings suggest that with the same MJO phase and time lag, AR activity may respond similarly or differently to concurrent El Niño/La Niña events. Further, the uncertainty on ENSO-AR relationship induced by different AR tracking algorithms and ENSO indices (Section 4.1) may also compound the responses of ARs to ENSO and MJO.

A similar analysis with the WRF simulations further confirms that interactions between different MJO and ENSO phases can lead to variegated responses of AR activity and AR precipitation (Figures 11 and 12). The percentages of AR frequency (and associated precipitation) agreement between El Niño-MJO and La Niña-MJO periods are 61% in ORWA, 48% in NCA, and 57% in SCA, respectively. In both MERRA2 and WRF, the agreement in ORWA AR anomalies between El Niño–MJO and La Niña–MJO periods increases with time lags ranging from five to one week following the MJO phases. In contrast, increased coherence between El Niño-MJO and La Niña-MJO conditions is not found in NCA and SCA. The complicated responses of AR activity to the interactions of ENSO and MJO are also reported by Mundhenk et al. (2016). Given that ENSO, MJO, and their concurrent effects offer predictive skill for winter precipitation (DelSole et al., 2017), employing the variegated AR responses to ENSO and MJO detected in the current study may further advance the prediction of ARs and precipitation across the western US.

5. Conclusions

To improve the prediction of western US hydroclimate at subseasonal-to seasonal-timescales, we examine the relationships between hydroclimate (including AR frequency and associated precipitation) and low-frequency climate variability (including ENSO and MJO) by using observations and a large ensemble of WRF simulations from 1981 to 2017. The large ensemble approach not only enables us to quantify climate mode-AR and AR-precipitation relationships by considering observations/modeling uncertainties due to internal climate variability, but also offers a physically based and systematic assessment of extreme ENSO events' modulation on landfalling ARs and precipitation. We find that WRF reproduces the spatial and temporal patterns of AR frequency, including the climatological mean and interannual variability. WRF also reproduces the mean and variability of seasonal total precipitation in the western US and the variability of AR precipitation, although it underestimates AR precipitation.

ENSO plays different roles in modulating AR activity at ocean basin, regional, and grid point scale. ENSO has small effects on the North Pacific basin-wide averaged AR activity and grid-scale ARs in the western US, but it influences ARs at regional scale. Specifically, AR activity is strengthened (weakened) along 30°N and weakened (strengthened) to its south and north during El Niño (La Niña and ENSO neutral) years, consistent with previous literature. When aggregating ARs over the western US, we discover that the ENSO-AR relationship depends on ENSO indices (ELI and Niño 3.4) and climate datasets (MERRA2 and WRF simulations), with the ELI identifying enhanced landfalling AR activity during extreme (or eastern Pacific)

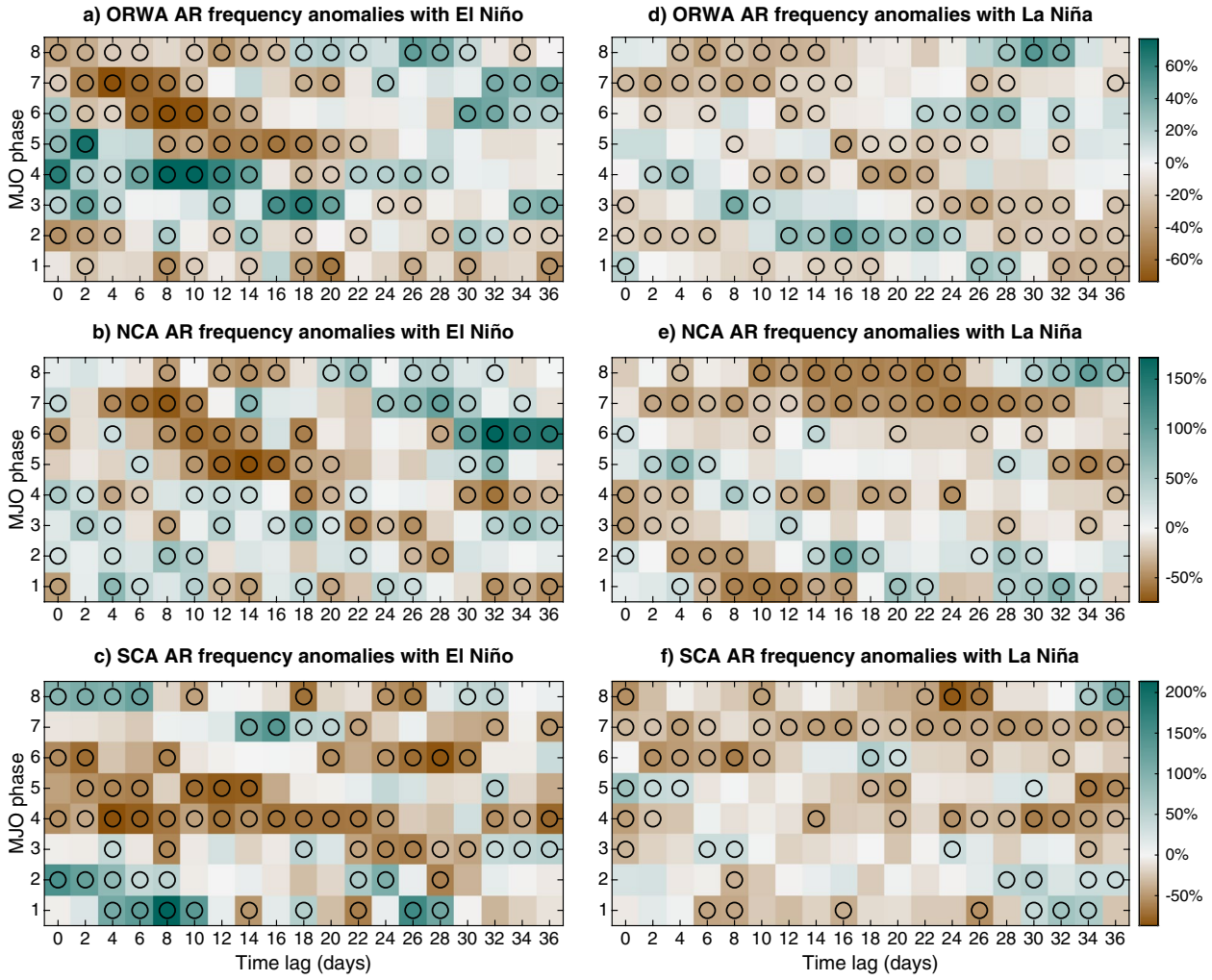

Figure 11. Anomalies in the Weather Research and Forecast (WRF) model simulated atmospheric river (AR) frequency (percentage difference in relative to all days in winter) by El Niño/Southern Oscillation type (a–c: El Niño, d–f: La Niña) and Madden-Julian oscillation (MJO) phase over (a, d) Oregon and Washington (ORWA), (b, e) northern California (NCA), and (c, f) southern California (SCA). Circle refers to a significant difference in AR frequency between respective MJO lagged days and all winter days using two sample *t*-test with the *p* values adjusted by controlling the false discovery rate at 0.05.

El Niño events in both datasets. The findings highlight ELI as a valuable source of seasonal predictability of landfalling ARs. While the responses of ORWA ARs to different ENSO phases are similar to NPNA ARs, NCA and SCA share close ENSO-AR relationship. Moreover, AR precipitation corresponds well with AR frequency by ENSO phase.

This study also shows a relationship between MJO and landfalling AR activity. MJO can lead to anomalously high/low AR frequency across the western US, depending on the phase of MJO and time lag. For example, AR frequency in ORWA decreases in the two weeks following MJO phases 1, 2, 7, and 8, but increases after phases 3–5 with the same time lags. In addition, the lack of statistically significant MJO-AR relationships in observations can be attributed to the small sample size, as the relationships are significant in the full set of WRF large-ensemble, but insignificant for a subset of the large-ensemble data. Furthermore, ENSO substantially modulates the MJO-AR relationship in both the large ensembles and observations, triggering variegated responses of landfalling ARs and AR precipitation in La Niña and El Niño years. If we compare El Niño-MJO and La Niña-MJO periods, only ~50% of their anomalies in AR frequency have the same sign (i.e., both positive or negative). With time lags ranging from 5 to 1 week following MJO phases, the agreement in ORWA AR anomalies between El Niño-MJO and La Niña-MJO periods increases, but the increased coherence is not found in NCA and SCA. A parallel analysis for AR

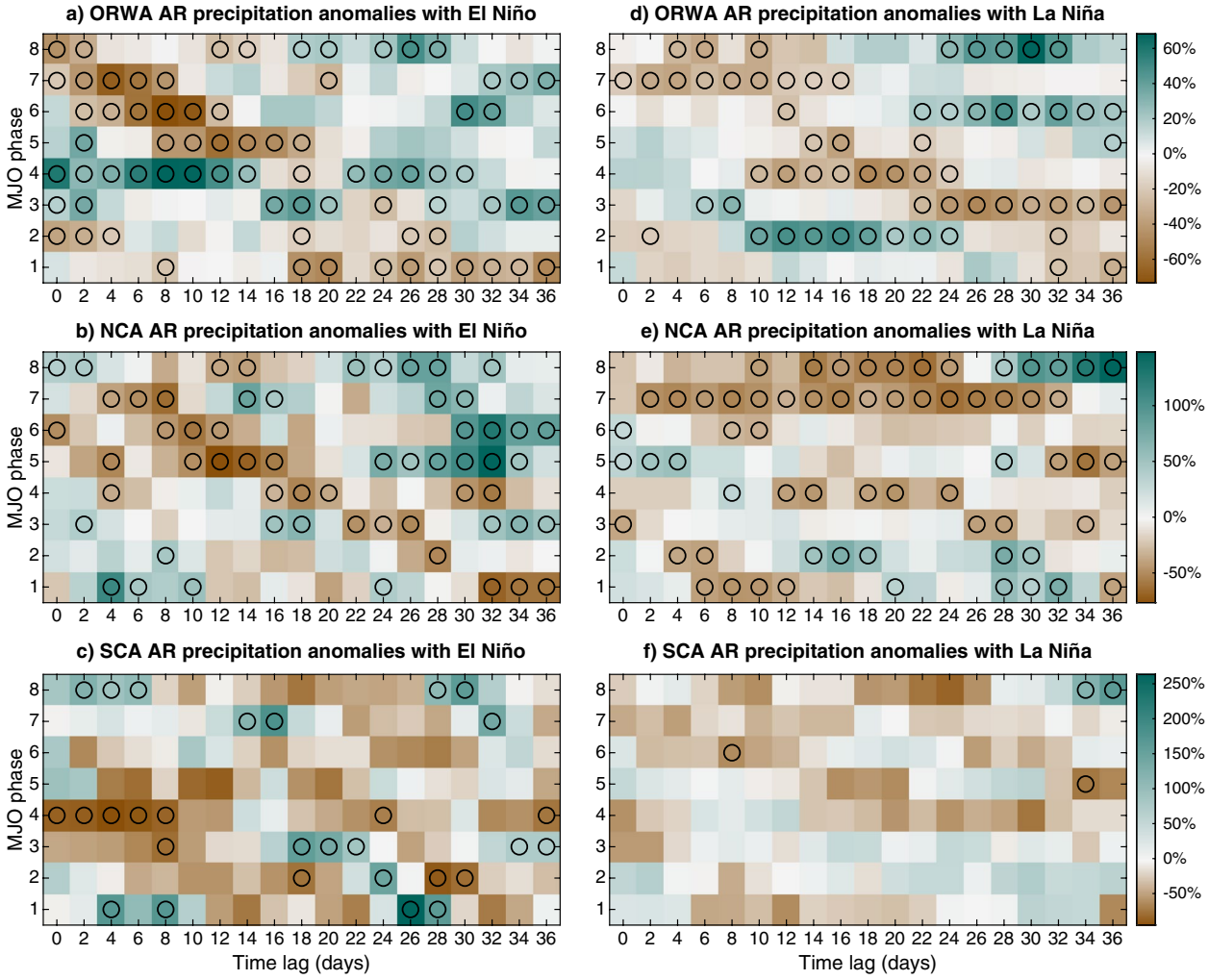

Figure 12. Anomalies in the Weather Research and Forecast (WRF) model simulated atmospheric river (AR) precipitation (percentage difference in relative to all days in winter) by El Niño/Southern Oscillation type (a–c: El Niño, d–f: La Niña) and Madden-Julian oscillation (MJO) phase over (a, d) Oregon and Washington (ORWA), (b, e) northern California (NCA), and (c, f) southern California (SCA). Circle refers to a significant difference in AR precipitation between respective MJO lagged days and all winter days using two sample *t*-test with the *p* values adjusted by controlling the false discovery rate at 0.05.

precipitation further confirms the joint influence of ENSO-MJO on AR precipitation. Our findings highlight the need for evaluating concurrent effects of different climate modes on ARs and precipitation, and may shed light on a path toward accurate subseasonal-to-seasonal prediction of ARs and precipitation over the western US.

Data Availability Statement

The MERRA-2 reanalysis is available through the NASA Goddard Earth Sciences Data Information Services Center (https://disc.gsfc.nasa.gov/datasets?keywords=%22MERRA-2%22&page=1&source=Models%2FAnalyses%20MERRA-2). CPC US Unified Precipitation data are provided by the NOAA/OAR/ESRL PSL, Boulder, Colorado, USA, from their website at https://psl.noaa.gov/. The PRISM precipitation data are provided by the PRISM climate group at the Oregon State University (https://prism.oregonstate.edu). The WRF data are publicly available through the NERSC portal (https://portal.nersc.gov/archive/home/projects/cascade/www/ARs_WesternUSprecip).

Acknowledgments
This material is based upon work supported by the U.S. Department of Energy, Office of Science, Office of Biological and Environmental Research, Climate and Environmental Sciences Division, Regional & Global Model Analysis Program, under Award Number DE-AC02-05CH11231. This research used resources of the National Energy Research Scientific Computing Center (NERSC), a U.S. Department of Energy Office of Science User Facility operated under Contract No. DE-AC02-05CH11231. We thank Travis A. O'Brien (Indiana University Bloomington and Lawrence Berkeley National Laboratory) for running the Tempest algorithm to detect atmospheric rivers and providing valuable insight into the analysis and interpretation of the climate data. The authors also thank Hari Krishnan (Lawrence Berkeley National Laboratory) for setting up the data portal on NERSC.

References

American Meteorological Society. (2019). *Atmospheric river - AMS glossary*. Retrieved from http://glossary.ametsoc.org/wiki/Atmospheric_river

Arcodia, M. C., Kirtman, B. P., & Siqueira, L. S. P. (2020). How MJO teleconnections and ENSO interference impacts U.S. precipitation. *Journal of Climate*, *33*, 4621–4640. https://doi.org/10.1175/JCLI-D-19-0448.1

Baggett, C. F., Barnes, E. A., Maloney, E. D., & Mundhenk, B. D. (2017). Advancing atmospheric river forecasts into subseasonal-to-seasonal time scales. *Geophysical Research Letters*, *44*, 7528–7536. https://doi.org/10.1002/2017GL074434

Capotondi, A., Wittenberg, A. T., Newman, M., Di Lorenzo, E., Yu, J. Y., Braconnot, P., et al. (2015). Understanding ENSO diversity. *Bulletin of the American Meteorological Society*, *96*, 921–938. https://doi.org/10.1175/BAMS-D-13-00117.1

Collow, A. B. M., Mersiovsky, H., & Bosilovich, M. G. (2020). Large-scale influences on atmospheric river–induced extreme precipitation events along the coast of Washington State. *Journal of Hydrometeorology*, *21*, 2139–2156. https://doi.org/10.1175/JHM-D-19-0272.1

Daly, C., Halbleib, M., Smith, J. I., Gibson, W. P., Doggett, M. K., Taylor, G. H., et al. (2008). Physiographically sensitive mapping of climatological temperature and precipitation across the conterminous United States. *International Journal of Climatology*, *28*, 2031–2064. https://doi.org/10.1002/joc.1688

DeFlorio, M. J., Waliser, D. E., Guan, B., Lavers, D. A., Martin Ralph, F., & Vitart, F. (2018). Global assessment of atmospheric river prediction skill. *Journal of Hydrometeorology*, *19*, 409–426. https://doi.org/10.1175/JHM-D-17-0135.1

DeFlorio, M. J., Waliser, D. E., Ralph, F. M., Guan, B., Goodman, A., Gibson, P. B., et al. (2019). Experimental subseasonal-to-seasonal (S2S) forecasting of atmospheric rivers over the western United States. *Journal of Geophysical Research: Atmospheres*, *124*, 11242–11265. https://doi.org/10.1029/2019JD031200

DelSole, T., Trenary, L., Tippett, M. K., & Pegion, K. (2017). Predictability of week-3-4 average temperature and precipitation over the contiguous United States. *Journal of Climate*. https://doi.org/10.1175/JCLI-D-16-0567.1

Deser, C., Lehner, F., Rodgers, K. B., Ault, T., Delworth, T. L., DiNezio, P. N., et al. (2020). Insights from Earth system model initial-condition large ensembles and future prospects. *Nature Climate Change*, *10*, 277–286. https://doi.org/10.1038/s41558-020-0731-2

Dettinger, M. D., Ralph, F. M., Das, T., Neiman, P. J., & Cayan, D. R. (2011). Atmospheric rivers, floods and the water resources of California. *Water*, *3*, 445–478. https://doi.org/10.3390/w3020445

Fonseca, R., Koh, T. Y., & Teo, C. K. (2019). Multi-scale interactions in a high-resolution tropical-belt experiment and observations. *Climate Dynamics*, *52*. https://doi.org/10.1007/s00382-018-4332-y

Gelaro, R., McCarty, W., Suárez, M. J., Todling, R., Molod, A., Takacs, L., et al. (2017). The modern-era retrospective analysis for research and applications, version 2 (MERRA-2). *Journal of Climate*, *30*, 5419–5454. https://doi.org/10.1175/JCLI-D-16-0758.1

Gershunov, A., Shulgina, T., Clemesha, R. E. S., Guirguis, K., Pierce, D. W., Dettinger, M. D., et al. (2019). Precipitation regime change in Western North America: The role of atmospheric rivers. *Scientific Reports*, *9*. https://doi.org/10.1038/s41598-019-46169-w

Gibson, P. B., Waliser, D. E., Guan, B., Deflorio, M. J., Ralph, F. M., & Swain, D. L. (2020). Ridging associated with drought across the western and southwestern United States: Characteristics, trends, and predictability sources. *Journal of Climate*, *33*. https://doi.org/10.1175/JCLI-D-19-0439.1

Gibson, P. B., Waliser, D. E., Lee, H., Tian, B., & Massoud, E. (2019). Climate model evaluation in the presence of observational uncertainty: Precipitation indices over the contiguous United States. *Journal of Hydrometeorology*, *20*. https://doi.org/10.1175/JHM-D-18-0230.1

Giorgetta, M. A., & Roeckner, E. (2002). Forcing of the quasi-biennial oscillation from a broad spectrum of atmospheric waves. *Geophysical Research Letters*, *29*. https://doi.org/10.1029/2002GL014756

Guan, B., & Waliser, D. E. (2015). Detection of atmospheric rivers: Evaluation and application of an algorithm for global studies. *Journal of Geophysical Research*, *120*. https://doi.org/10.1002/2015JD024257

Guan, B., Waliser, D. E., Molotch, N. P., Fetzer, E. J., & Neiman, P. J. (2012). Does the Madden-Julian oscillation influence wintertime atmospheric rivers and snowpack in the Sierra Nevada? *Monthly Weather Review*, *140*. https://doi.org/10.1175/MWR-D-11-00087.1

Hagos, S., Feng, Z., Landu, K., & Long, C. N. (2015). Advection, moistening, and shallow-to-deep convection transitions during the initiation and propagation of Madden-Julian oscillation. *Journal of Advances in Modeling Earth Systems*, *6*. https://doi.org/10.1002/2014MS000335

Hagos, S., Feng, Z., Mcfarlane, S., & Leung, L. R. (2013). Environment and the lifetime of tropical deep convection in a cloud-permitting regional model simulation. *Journal of the Atmospheric Sciences*, *70*. https://doi.org/10.1175/JAS-D-12-0260.1

Hagos, S., & Leung, L. R. (2011). Moist thermodynamics of the Madden-Julian oscillation in a cloud-resolving simulation. *Journal of Climate*, *24*. https://doi.org/10.1175/2011JCLI4212.1

Hagos, S., Leung, L. R., Yang, Q., Zhao, C., & Lu, J. (2015). Resolution and dynamical core dependence of atmospheric river frequency in global model simulations. *Journal of Climate*, *28*. https://doi.org/10.1175/JCLI-D-14-00567.1

Hagos, S. M., Leung, L. R., Yoon, J. H., Lu, J., & Gao, Y. (2016). A projection of changes in landfalling atmospheric river frequency and extreme precipitation over western North America from the Large Ensemble CESM simulations. *Geophysical Research Letters*, *43*. https://doi.org/10.1002/2015GL067392

Harris, S. M., & Carvalho, L. M. V. (2018). Characteristics of southern California atmospheric rivers. *Theoretical and Applied Climatology*, *132*. https://doi.org/10.1007/s00704-017-2138-1

Henderson, S. A., Maloney, E. D., & Barnes, E. A. (2016). The influence of the Madden-Julian oscillation on Northern Hemisphere winter blocking. *Journal of Climate*, *29*. https://doi.org/10.1175/JCLI-D-15-0502.1

Huang, H., Winter, J. M., Osterberg, E. C., Hanrahan, J., Bruyère, C. L., Clemins, P., & Beckage, B. (2020). Simulating precipitation and temperature in the Lake Champlain basin using a regional climate model: Limitations and uncertainties. *Climate Dynamics*, *54*. https://doi.org/10.1007/s00382-019-04987-8

Jin, F., & Hoskins, B. J. (1995). The direct response to tropical heating in a baroclinic atmosphere. *Journal of the Atmospheric Sciences*, *52*, 307–319. https://doi.org/10.1175/1520-0469(1995)052<0307:tdrtth>2.0.co;2

Johnson, N. C., Collins, D. C., Feldstein, S. B., L'heureux, M. L., & Riddle, E. E. (2014). Skillful wintertime North American temperature forecasts out to 4 weeks based on the state of ENSO and the MJO. *Weather and Forecasting*, *29*. https://doi.org/10.1175/WAF-D-13-00102.1

Kim, H. M., Zhou, Y., & Alexander, M. A. (2017). Changes in atmospheric rivers and moisture transport over the Northeast Pacific and western North America in response to ENSO diversity. *Climate Dynamics*, *52*, 7375–7388. https://doi.org/10.1007/s00382-017-3598-9

Kim, J., Guan, B., Waliser, D. E., Ferraro, R. D., Case, J. L., Iguchi, T., et al. (2018). Winter precipitation characteristics in western US related to atmospheric river landfalls: Observations and model evaluations. *Climate Dynamics*, *50*, 231–248. https://doi.org/10.1007/s00382-017-3601-5

Kuma, K.-I. (1990). A quasi-biennial oscillation in the intensity of the intra-seasonal oscillation. *International Journal of Climatology*, *10*. https://doi.org/10.1002/joc.3370100304

Lavers, D. A., & Villarini, G. (2015). The contribution of atmospheric rivers to precipitation in Europe and the United States. *Journal of Hydrology*, *522*. https://doi.org/10.1016/j.jhydrol.2014.12.010

Leung, L. R., & Qian, Y. (2009). Atmospheric rivers induced heavy precipitation and flooding in the western U.S. simulated by the WRF regional climate model. *Geophysical Research Letters*, *36*. https://doi.org/10.1029/2008GL036445

Madden, R. A., & Julian, P. R. (1971). Detection of a 40–50 Day Oscillation in the Zonal Wind in the Tropical Pacific. *Journal of the Atmospheric Sciences*, *28*. https://doi.org/10.1175/1520-0469(1971)028<0702:DOADOI>2.0.CO;2

Madden, R. A., & Julian, P. R. (1972). Description of global-scale circulation cells in the tropics with a 40–50 day period. *Journal of the Atmospheric Sciences*, *29*. https://doi.org/10.1175/1520-0469(1972)029<1109:DOGSCC>2.0.CO;2

Martin, A., Ralph, F. M., Demirdjian, R., DeHaan, L., Weihs, R., Helly, J., et al. (2018). Evaluation of atmospheric river predictions by the WRF model using aircraft and regional mesonet observations of orographic precipitation and its forcing. *Journal of Hydrometeorology*, *19*. https://doi.org/10.1175/JHM-D-17-0098.1

Martin, Z., Wang, S., Nie, J., & Sobel, A. (2019). The impact of the QBO on MJO convection in cloud-resolving simulations. *Journal of the Atmospheric Sciences*, *76*. https://doi.org/10.1175/JAS-D-18-0179.1

Mundhenk, B. D., Barnes, E. A., & Maloney, E. D. (2016). All-season climatology and variability of atmospheric river frequencies over the North Pacific. *Journal of Climate*, *29*. https://doi.org/10.1175/JCLI-D-15-0655.1

Mundhenk, B. D., Barnes, E. A., Maloney, E. D., & Baggett, C. F. (2018). Skillful empirical subseasonal prediction of landfalling atmospheric river activity using the Madden–Julian oscillation and quasi-biennial oscillation. *npj Climate and Atmospheric Science*, *1*. https://doi.org/10.1038/s41612-017-0008-2

Nardi, K. M., Baggett, C. F., Barnes, E. A., Maloney, E. D., Harnos, D. S., & Ciasto, L. M. (2020). Skillful all-season s2s prediction of U.S. precipitation using the MJO and QBO. *Weather and Forecasting*, *35*. https://doi.org/10.1175/WAF-D-19-0232.1

Orbe, C., van Roekel, L., Adames, Á. F., Dezfuli, A., Fasullo, J., Gleckler, P. J., et al. (2020). Representation of modes of variability in six U.S. climate models. *Journal of Climate*, *33*. https://doi.org/10.1175/JCLI-D-19-0956.1

Pan, B., Hsu, K., Aghakouchak, A., Sorooshian, S., & Higgins, W. (2019). Precipitation prediction skill for the west coast United States: From short to extended range. *Journal of Climate*, *32*. https://doi.org/10.1175/JCLI-D-18-0355.1

Patricola, C. M., O'Brien, J. P., Risser, M. D., Rhoades, A. M., O'Brien, T. A., Ullrich, P. A., et al. (2020). Maximizing ENSO as a source of western US hydroclimate predictability. *Climate Dynamics*, *54*. https://doi.org/10.1007/s00382-019-05004-8

Patricola, C. M., Saravanan, R., & Chang, P. (2014). The impact of the El Niño-Southern oscillation and Atlantic meridional mode on seasonal Atlantic tropical cyclone activity. *Journal of Climate*, *27*. https://doi.org/10.1175/JCLI-D-13-00687.1

Payne, A. E., Demory, M.-E., Leung, L. R., Ramos, A. M., Shields, C. A., Rutz, J. J., et al. (2020). Responses and impacts of atmospheric rivers to climate change. *Nature Reviews Earth & Environment*, *1*. https://doi.org/10.1038/s43017-020-0030-5

Payne, A. E., & Magnusdottir, G. (2014). Dynamics of landfalling atmospheric rivers over the North Pacific in 30 years of MERRA reanalysis. *Journal of Climate*, *27*. https://doi.org/10.1175/JCLI-D-14-00034.1

Powers, J. G., Klemp, J. B., Skamarock, W. C., Davis, C. A., Dudhia, J., Gill, D. O., et al. (2017). The weather research and forecasting model: overview, system efforts, and future directions. *Bulletin of the American Meteorological Society*, *98*, 1717–1737. https://doi.org/10.1175/bams-d-15-00308.1

Reynolds, R. W., Rayner, N. A., Smith, T. M., Stokes, D. C., & Wang, W. (2002). An improved in situ and satellite SST analysis for climate. *Journal of Climate*, *15*. https://doi.org/10.1175/1520-0442(2002)015<1609:AIISAS>2.0.CO;2

Richter, J. H., Anstey, J. A., Butchart, N., Kawatani, Y., Meehl, G. A., Osprey, S., & Simpson, I. R. (2020). Progress in simulating the quasi-biennial oscillation in CMIP models. *Journal of Geophysical Research: Atmospheres*, *125*. https://doi.org/10.1029/2019JD032362

Richter, J. H., Solomon, A., & Bacmeister, J. T. (2014). On the simulation of the quasi-biennial oscillation in the community atmosphere model, version 5. *Journal of Geophysical Research*, *119*. https://doi.org/10.1002/2013JD021122

Roundy, P. E., MacRitchie, K., Asuma, J., & Melino, T. (2010). Modulation of the global atmospheric circulation by combined activity in the Madden-Julian oscillation and the El Niño-southern oscillation during boreal winter. *Journal of Climate*, *23*. https://doi.org/10.1175/2010JCLI3446.1

Rutz, J. J., James Steenburgh, W., & Martin Ralph, F. (2014). Climatological characteristics of atmospheric rivers and their inland penetration over the western united states. *Monthly Weather Review*, *142*. https://doi.org/10.1175/MWR-D-13-00168.1

Rutz, J. J., Shields, C. A., Lora, J. M., Payne, A. E., Guan, B., Ullrich, P., et al. (2019). The atmospheric river tracking method intercomparison project (ARTMIP): Quantifying uncertainties in atmospheric river climatology. *Journal of Geophysical Research: Atmospheres*, *124*. https://doi.org/10.1029/2019JD030936

Rutz, J. J., & Steenburgh, W. J. (2012). Quantifying the role of atmospheric rivers in the interior western United States. *Atmospheric Science Letters*, *13*. https://doi.org/10.1002/asl.392

Sellars, S. L., Gao, X., & Sorooshian, S. (2015). An object-oriented approach to investigate impacts of climate oscillations on precipitation: A western United States case study. *Journal of Hydrometeorology*, *16*. https://doi.org/10.1093/obo/9780195396577-0278

Shields, C. A., & Kiehl, J. T. (2016). Simulating the Pineapple Express in the half degree Community Climate System Model, CCSM4. *Geophysical Research Letters*, *43*, 7767–7773. https://doi.org/10.1002/2016GL069476

Shields, C. A., Rutz, J. J., Leung, L. Y., Martin Ralph, F., Wehner, M., Kawzenuk, B., et al. (2018). Atmospheric River tracking method Intercomparison Project (ARTMIP): Project goals and experimental design. *Geoscientific Model Development*, *11*, 2455–2474. https://doi.org/10.5194/gmd-11-2455-2018

Stan, C., Straus, D. M., Frederiksen, J. S., Lin, H., Maloney, E. D., & Schumacher, C. (2017). Review of tropical-extratropical teleconnections on intraseasonal time scales. *Reviews of Geophysics*, *55*. https://doi.org/10.1002/2016RG000538

Swain, D. L., Langenbrunner, B., Neelin, J. D., & Hall, A. (2018). Increasing precipitation volatility in twenty-first-century California. *Nature Climate Change*, *8*, 427–433. https://doi.org/10.1038/s41558-018-0140-y

Ullrich, P. A., & Zarzycki, C. M. (2017). TempestExtremes: A framework for scale-insensitive pointwise feature tracking on unstructured grids. *Geoscientific Model Development*, *10*, 1069–1090. https://doi.org/10.5194/gmd-2016-217-ac2

Wang, S., Sobel, A. H., & Nie, J. (2016). Modeling the MJO in a cloud-resolving model with parameterized large-scale dynamics: Vertical structure, radiation, and horizontal advection of dry air. *Journal of Advances in Modeling Earth Systems*, *8*. https://doi.org/10.1002/2015MS000529

Wang, S. Y., Yoon, J. H., Becker, E., & Gillies, R. (2017). California from drought to deluge. *Nature Climate Change*, *7*, 465–468. https://doi.org/10.1038/nclimate3330

Wheeler, M. C., & Hendon, H. H. (2004). An all-season real-time multivariate MJO index: Development of an index for monitoring and prediction. *Monthly Weather Review*, *132*. https://doi.org/10.1175/1520-0493(2004)132<1917:AARMMI>2.0.CO;2

Wilks, D. S. (2016). "The stippling shows statistically significant grid points": How research results are routinely overstated and overinterpreted, and what to do about it. *Bulletin of the American Meteorological Society*, *97*. https://doi.org/10.1175/BAMS-D-15-00267.1

Williams, I. N., & Patricola, C. M. (2018). Diversity of ENSO events unified by convective threshold sea surface temperature: A nonlinear ENSO index. *Geophysical Research Letters*, *45*. https://doi.org/10.1029/2018GL079203

Xie, P., Chen, M., & Shi, W. (2010). CPC unified gauge-based analysis of global daily precipitation. *Preprints, 24th conference on hydrology*. Atlanta, GA: American Meteorological Society. Retrieved from https://ams.confex.com/ams/90annual/techprogram/paper_163676.htm

Yoo, C., & Son, S. W. (2016). Modulation of the boreal wintertime Madden-Julian oscillation by the stratospheric quasi-biennial oscillation. *Geophysical Research Letters*, *43*. https://doi.org/10.1002/2016GL067762

Zhang, C. (2005). Madden-Julian oscillation. *Reviews of Geophysics*, *43*. https://doi.org/10.1029/2004RG000158

Zhou, Y., & Kim, H. M. (2018). Prediction of atmospheric rivers over the North Pacific and its connection to ENSO in the North American multi-model ensemble (NMME). *Climate Dynamics*, *51*, 1623–1637. https://doi.org/10.1007/s00382-017-3973-6

Zhou, Y., O'brien, T., Ullrich, P., Collins, W., Patricola, C., & Rhoades, A. (2020). Uncertainties in atmospheric river life cycles by detection algorithms: Climatology and variability. *Earth and Space Science Open Archive* https://doi.org/10.1002/ESSOAR.10504174.1

Zhu, Y., & Newell, R. E. (1998). A proposed algorithm for moisture fluxes from atmospheric rivers. *Monthly Weather Review*, *126*. https://doi.org/10.1175/1520-0493(1998)126<0725:APAFMF>2.0.CO;2